BARD

FINAL REPORT

PROJECT NO. US-1759-89

Spray Target Architecture and Turbulent Transport in Air-Carrier Pesticide Application Systems

D.K. Giles, M. J. Delwiche, H. Frankel, A. Grinstein, M. Austerweil

1994

42108 D

Standard BARD Cover Page for Scientific Reports

Date: March 20, 1994

BARD
P.O.Box 6
Bet-Dagan, ISRAEL

BARD Project No. US 1759-89

Title

Spray Target Architecture and Turbulent Transport in Air-Carrier Pesticide Application Systems

Investigators' Names (Principal listed first)	Investigator's Institutions
Durham K. Giles	University of Calif., Davis
Michael J. Delwiche	University of Calif., Davis
Harry Frankel	ARO, Volcani Center
Avi Grinstein	ARO, Volcani Center
Miriam Austerweil	ARO, Volcani Center

Project's starting date: July 20, 1990

Type of Report: 1st annual _____ 2nd Annual _____ Final X

Signature
Principal Investigator

Signature
Institution's Authorizing Official

Spray Target Architecture and Turbulent Transport in Air-Carrier Pesticide Application Systems

BARD Project No. US-1759-89

Table of Contents

ABSTRACT

A fluid-dynamic technique was developed to control velocity, turbulence and shape of an air jet emitted from an internal-mixing, air-atomization nozzle. Small, control jets were positioned immediately downstream from the nozzle exit and injected air into the main spray jet leaving the nozzle. Main jet, i.e., the spray-carrying air jet, characteristics were controlled by varying the diameter and mass flow rates from the control jets. The technique could provide control of jet velocity over 2 - 4 turndown ratio, create uniform turbulence intensities of about 35 to 45 % over the flow field and increase the planar area covered by the jet by two- to three-fold. While the control technique was effective, it required significant air mass and pneumatic power input.

Air jet penetration into plant canopies and resulting foliar deposition of entrained spray droplets was experimentally investigated. Foliar area and density characteristics of the canopy were measured and equations relating accumulated area and density to depth of the canopy were developed. The air-atomizing nozzle, with the control jet systems, was used to spray a bed of chrysanthemum plants. Air penetration was measured by a high-speed, hot-film anemometry system with velocity probes positioned within the canopy. Spray deposition was measured by tracer analysis. A first order exponential decay, analogous to radiation extinction, described air jet movement into the canopy and spray deposition along the vertical axis. The relative extinction rate of spray deposition was generally higher than the extinction rate of air penetration. Spray deposition in lower regions of the plant was typically one order of magnitude less than deposition in upper regions of the plant.

Objectives:

The objectives of this project, as originally proposed were, :

1. To quantify the interactions between spray target foliar architecture, air-carrier turbulent characteristics, penetration of the air-jet into the canopy and the subsequent deposition of liquid spray droplets. Particularly, to determine optimal air-carrier characteristics for maximum uniformity and quantity of spray deposit.

2. To develop actuators to control velocity and the characteristic shape, length scale and intensity of turbulence with air-carriers to achieve optimal canopy penetration and spray deposition characteristics.

Scientific Work:

Phase 1. Development of a jet control technique for a pneumatic spray nozzle (Objective 2)

Background. In the air-carrier chemical application process, the type of crop being sprayed, the stage of crop growth or location of the target pest could require site, seasonal or instantaneous alterations of the flow characteristics and shape of the spray pattern. The flow characteristics and shape of the spray cloud determine the deposition pattern and deposition efficiency of the liquid spray droplets. The typical approach has been to design and develop spray control systems which regulate only the sprayer output. However, air-atomizing nozzles typically employ compressed air for atomization and transport of the spray liquid. The balance between flow of air and liquid is a critical factor for proper and desirable atomization. Therefore, for a given nozzle arrangement, any attempt to mechanically alter the flow characteristics of the air jet could consequently alter the liquid spray flow and atomization characteristics.

Another example of required alterations are the width and shape of the spray cloud from a circular pattern to a flat pattern and vice-versa. Commercial air-atomizing nozzles are typically configured to produce a round or flat pattern and the changing between patterns is only possible by replacing nozzles or nozzle air cap components. This operation not only affects the spray pattern, the projection of spray cloud and the internal flow characteristics of the nozzle but also it requires that the spray operation be stopped, the sprayer shutoff, all the sprayer boom nozzles disassembled, the air cap components replaced and then the nozzles reassembled.

Goals. The goals of this phase of the project were to: 1) develop a non-invasive, fluid-dynamic controller for a single source air-atomization nozzle to achieve control of the velocity and shape of the emitted jet; 2) experimentally characterize the flow field produced by the stationary nozzle under normal and controlled operating conditions; 3) determine the effects of

the control on the velocity, turbulence and shape of the emitted jet by comparing the experimental results with mathematical models and previous experimental data for single source turbulent air jets; 4) determine the air and power input requirements of the nozzle-controller system.

Nozzle-Controller System. The air-atomization nozzle used in this work and a prototype of the controller are shown in Figure 1. The nozzle assembly was a commercially produced spray head for green house and row crop pesticide application systems and based on a typical industrial round spray pattern design (1/4 J series, Spraying Systems Inc., Wheaton,IL) consisting of a coaxial nozzle to which liquid and atomizing air are supplied.

The controller consisted of two air jets facing each other, embedded in a nozzle shroud which was positioned immediately downstream of the conventional air cap of the nozzle and replacing the conventional shroud. The shroud was designed such that the controller jets were positioned 2 mm in both horizontal and vertical directions from the lip of the nozzle exit and were perpendicular to the main (spray) jet. In operation, atomizing air and spray liquid are supplied to the nozzle in the normal manner. The controller required only an additional air input at pressures less than one half that of the atomizing air. The flow from the control jets impinges and penetrates the main jet flow exiting from the nozzle outlet. At low control jet air flows, the control jet flow was expected to perturb the main jet flow and alter the ambient air entrainment into the edges of the main jet. At higher control jet flows, the momentum of the control jets was expected to inflict a distortion of both the shape and the flow characteristics of the main jet. These expectations were based on the work of Davis (1982) who investigated the method as a noise abatement technique for large mass jets. Two relative sizes of the controller air exits (designated as D/2 and D/1) were investigated. The designation refers to the ratio of the controller jet exit diameter to the nozzle jet exit diameter. D/1 indicates that the nozzle jet and controller jet have equal exit diameter and D/2 indicates that the diameter of the controller jet exit was one-half that of the nozzle jet exit making the exit area of the D/2 controller be 25 % that of the D/1 controller. An air atomization nozzle with conventional shroud attached and prototype controller jet shrouds for both controller jet sizes is also shown in Figure 2.

Experimental Apparatus and Procedure. Air pressure and mass flow rate inputs into the nozzle and controller were monitored using precision Bourdon tube test gauges and precision variable tube area rotameters. The turbulent flow field produced by the nozzle was characterized using a hot film anemometer and four constant temperature bridges interfaced to a digital data acquisition system card supported by a microcomputer. Each bridge maintained a single sensor, fiber film probe at 320 ^{o}C, corresponding to an overheat ratio of about 1.4.

Sampling rates were set at 1 kHz for sampling periods of 8 seconds for all channels. The sampling frequency was determined by monitoring the flow field with a power spectrum analyzer

that indicated that the flow field had significant frequencies of about 0.5 kHz. A sampling period of 8 seconds was found to achieve stationary data.

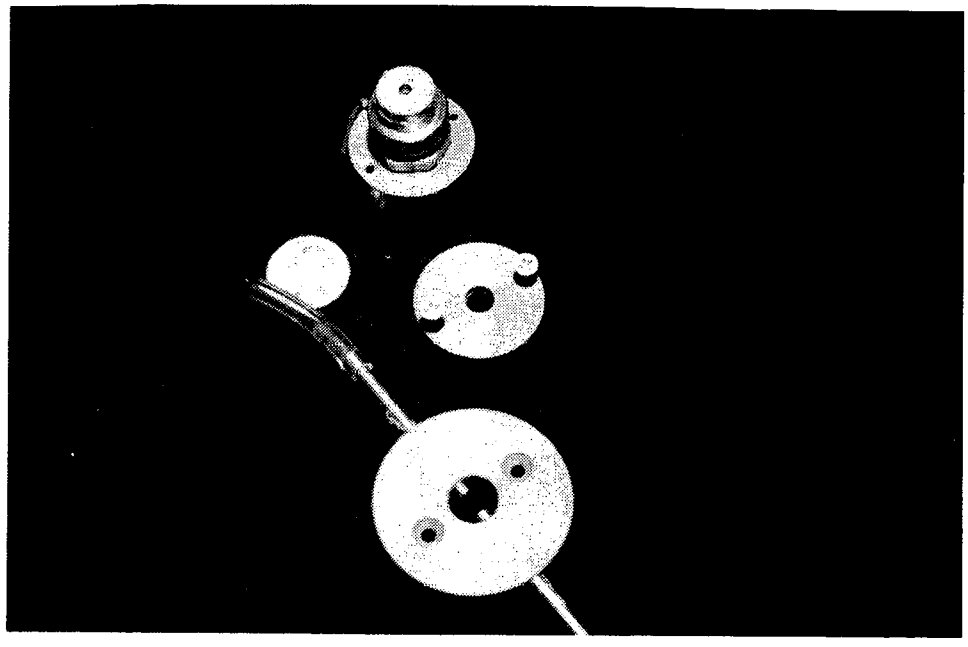

Figure 1. Air atomization nozzle (top), typical nozzle shroud (center), and controller jet nozzle shroud (bottom)

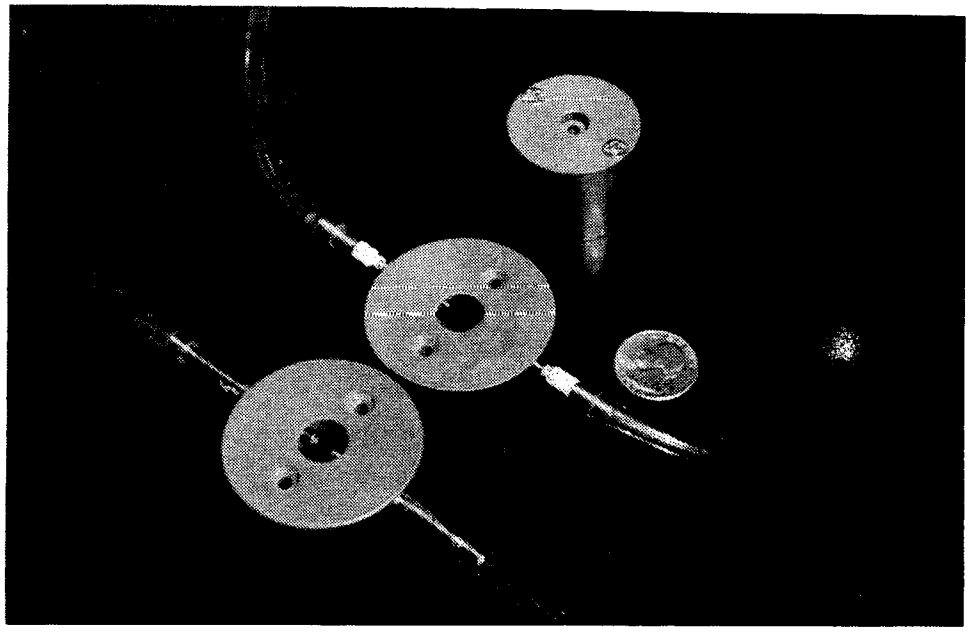

Figure 2. Air-atomization nozzle with conventional (non-control) shroud (top); D/2 controller jet shroud (middle); D/1 controller jet shroud (bottom).

The nozzle and controller were positioned 2.5 m above the laboratory floor and the emitted air jet was directed vertically downward. A He-Ne laser was placed on the floor and a mirror set against the face of the nozzle assembly to vertically align the nozzle and establish a reference center line for the flow originating at the nozzle exit outlet.

The flow field characterization consisted of velocity measurements along the main jet centerline from 0.10 to 0.90 m downstream of the nozzle and local flow field shape measurements over a 0.24 m by 0.24 m square grid, centered by the nozzle reference axis, at two distances from the nozzle exit; 0.30 m and 0.60 m. Measurements of the centerline velocities were made using a circular support which held the four probes within a 1 cm radius circle of the flow centerline. The circular support was vertically displaced along the nozzle centerline by means of a precision micropositioner with a resolution of 10 μm. The off-center flow field measurements were made by scanning with a computer controlled, two-axis precision positioning table. Both setups are shown in Figures 3 and 4. The nozzle was operated at main air jet pressures of 200, 275 and 350 kPa and controller air-jet pressures of 0, 30, 60 and 90 kPa. During all tests of flow field characterization, no liquid was supplied to the spray head. Addition of the liquid phase into the flow would have prevented the use of hot-film anemometry. Abramovich (1963) theoretically analyzed and discussed the specific case of a single port pneumatic atomizer with liquid-to-air mass ratios of the order of 1 and air-to-liquid volume ratios of the order of 1000 which were similar to the air-atomizer in the experiment. He concluded that such jets could be treated as gaseous, even for very large initial concentration of the liquid admixture since changes in the relative density of the jet flow were small and became even less important as ambient air was entrained into the jet as it moved downstream.

Nozzle-Controller System Flow. The rotameter readings of volumetric flow rates input to the nozzle and to each of the controller jets at each of the operating gauge pressures are shown in Table 1. It is common in industry to express rotameter volumetric flow rates at standard conditions of pressure (P_S = 100 kPa), temperature (T_S = 295 K), and density (ρ_S = 1. 200 kg/m^3) by the orifice equation:

$$Q_s = Q_o \sqrt{\frac{P_o + P_s}{P_s}} \left(\frac{T_s}{T_o + 273}\right), \qquad (1)$$

and then calculate the mass flow rate as:

$$m = \rho_s Q_s, \qquad (2)$$

where Q_S, P_S, T_S, and ρ_S are the volumetric flow rate in m^3/s, the pressure in kPa, the temperature in K, and the density in kg/m^3, respectively at standard conditions. Q_O, P_O, and T_O are the volumetric flow rate, the operating gauge pressure, and the temperature in ^{O}C,

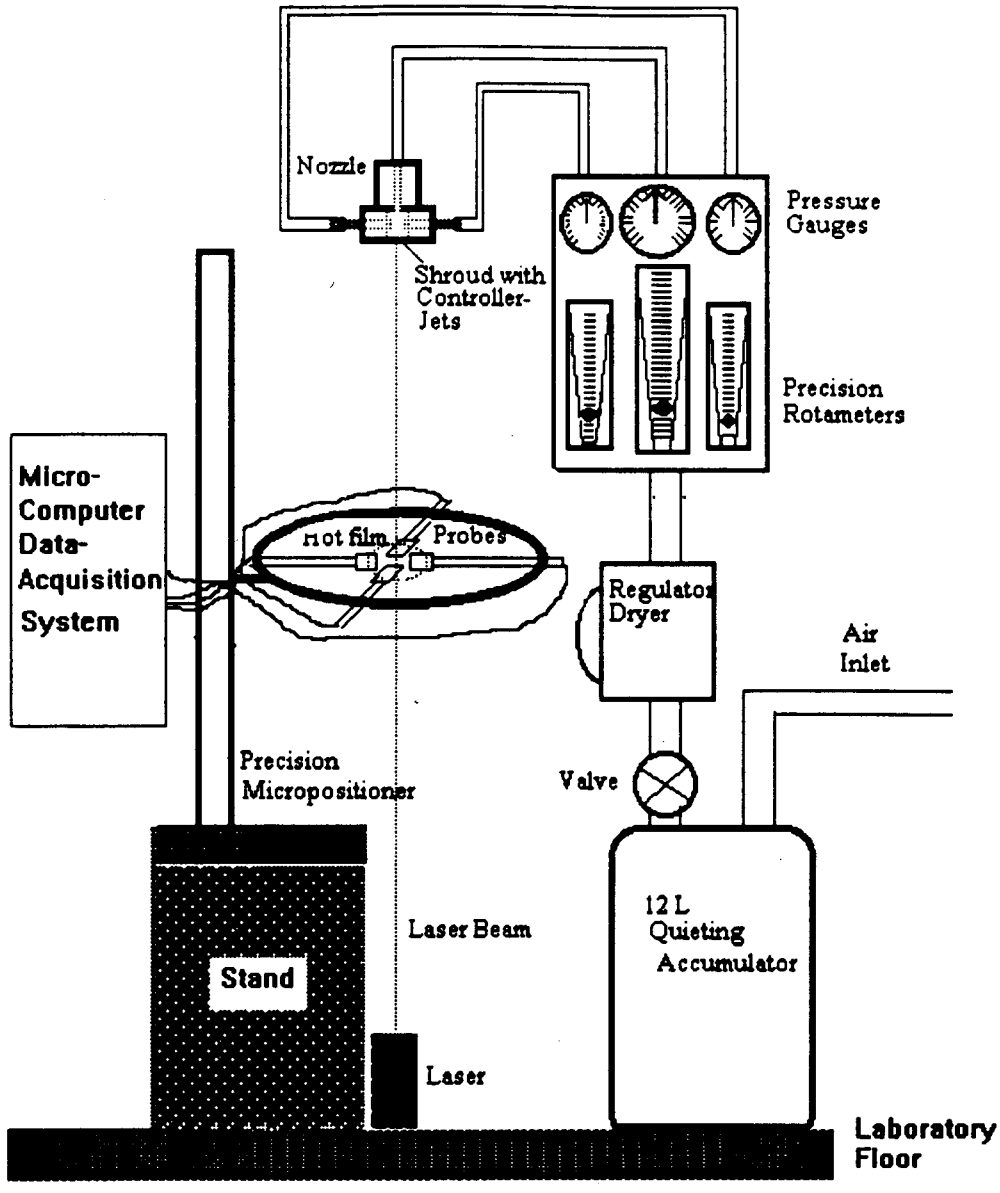

Figure 3. Experimental setup for the flow field centerline measurements.

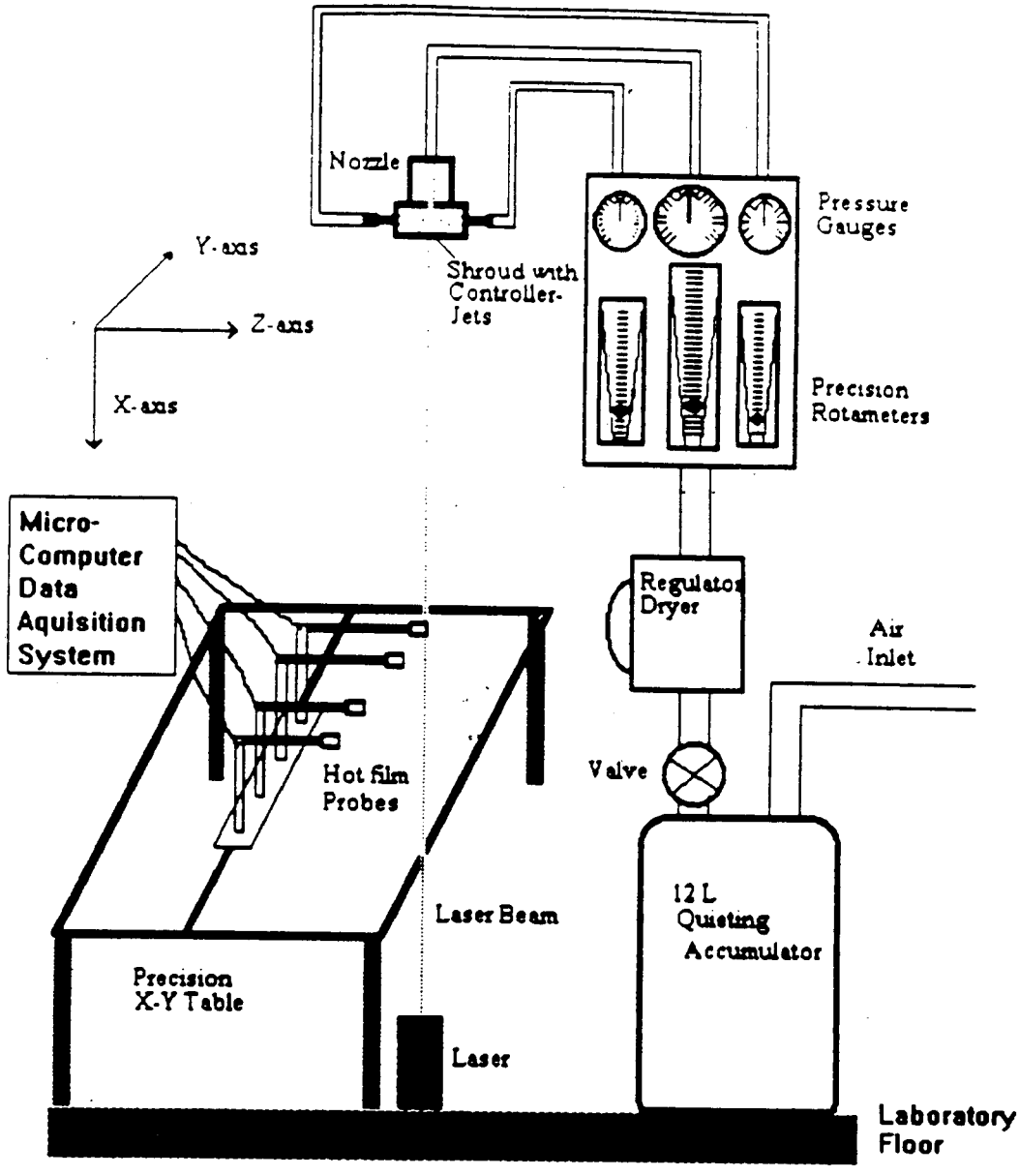

Figure 4. Experimental setup for flow field local profile and shape measurements.

respectively at operating conditions. m_x, is the mass flow rate in kg/s. The volumetric and mass flow rates calculated based on equations 1 and 2 are shown in Table 1. It is more accurate to calculate the flow rates input to the system from the state equation of compressible flow:

$$P = \rho R T, \tag{3}$$

where P is the absolute flow pressure in kPa, ρ is the corresponding flow density in kg/m^3, R is the gas constant for air (287 m^2/(s^2 K),) and T is the flow temperature in K. Equation 3 was used to calculate air densities at different operating pressures, then the mass flow rates were calculated as the product of volumetric flow rates and air densities. The results are also shown in Table 1.

Comparison of mass flow rates determined by both methods shows a good agreement of the controller-jet pipe mass flow rates, but not as good an agreement of the main-jet nozzle mass flow rates, most likely due to the fact that in order to use the orifice equation, industrial applications assume that the rotameter outlet flows into the ambient air. However for the present case of application, the rotameter flows into a pressure gage, then into the nozzle, then into ambient air.

Main-Jet Nozzle Flow. Being a compressible fluid, air flow is commonly treated by isentropic compressible flow theory. White (1986) presented a study of compressible flow from nozzles. The study indicated that the Mach number (defined as Ma = $\frac{V}{a}$, where V is the flow velocity and a is the sound velocity) is the dominant parameter in compressible flow. Theoretically, the flow was defined as subsonic if Ma is less than 1 and supersonic otherwise. This section is not intended as a rigorous treatment of incompressible nozzle-flow theory, its purpose is to use some tool equations from White (1986) to determine the flow regime of the nozzle-controller system used in this study.

Following are the one-dimensional isentropic-flow approximation equations and numbers applicable to the present case:

Mach number relations:

$$\frac{p_0}{p} = (1 + 0.2Ma^2)^{7/2}, \tag{4}$$

$$\frac{A}{A^*} = \frac{1}{Ma}\frac{(1+0.2Ma^2)^3}{1.728}, \tag{5}$$

Normal shock wave:

$$\frac{p_2}{p_1} = \frac{1}{\gamma+1}[2\gamma M_{a1}^2 - (\gamma - 1)], \tag{6}$$

Table 1. Nozzle-Controller Flow Parameters

Operating Gauge Pressures kPa	Rotameter Flow rate Readings 10^{-4} m^3/s	Orifice Mass Flow Rate g/s	*Actual Mass Flow Rate g/s	**Exit Volume. Flow Rate 10^{-4} m^3/s	**Exit Air Velocity m/s	Exit Reynolds Number
			Main-Jet Nozzle			
200	8.88	1.88	3.15	26.25	263	$6.2\ 10^4$
275	9.97	2.36	4.42	36.84	368	$8.7\ 10^4$
350	10.83	2.80	5.76	48.00	480	$11.4\ 10^4$
			D/1 Controller			
30	6.63	0.92	1.02	8.50	85	$2.0\ 10^4$
30	8.76	1.35	1.66	13.83	138	$3.3\ 10^4$
90	9.92	1.67	2.23	18.58	186	$4.4\ 10^4$
			D/2 Controller			
30	3.07	0.43	0.47	3.92	157	$1.8\ 10^4$
60	4.10	0.64	0.78	6.50	260	$3.1\ 10^4$
90	4.72	0.80	1.06	8.83	353	$4.2\ 10^4$

*Calculated based on rotameter readings and air densities at operating conditions of pressure and temperature.
** Calculated based on laboratory room (standard) conditions of pressure and temperature.

Critical values at sonic point: $\frac{p^*}{p} = 0.528,$ (7)

Maximum mass flow rate at choking : $m_{\max} = \frac{0.685\, p_o A_t}{(RT_o)^{1/2}},$ (8)

where A and A^* are the exit and throat areas of the nozzle in m^2, a is the speed of sound in m/s, and γ is the gas constant which, for air, is equal to 1.4, and Ma is the dimensionless Mach number.

The nozzle is shown in Figure 5. It is shown to have a converging-diverging geometry with an exit-to-throat area ratio equal to 2.05, steady absolute operating pressures of 300, 375, and 450 kPa, a constant absolute back pressure of 100 kPa, and a constant temperature of 295 ^oK. The back-to-operating pressure ratios as given by equation 7 are 0.334, 0.267, and 0.223. All ratios being less than 0.528, indicate that all nozzle operating pressures caused supersonic

flow at the throat. At the given area ratio of 2.05, the design Mach number was found from equation 5 equal to 2.23.

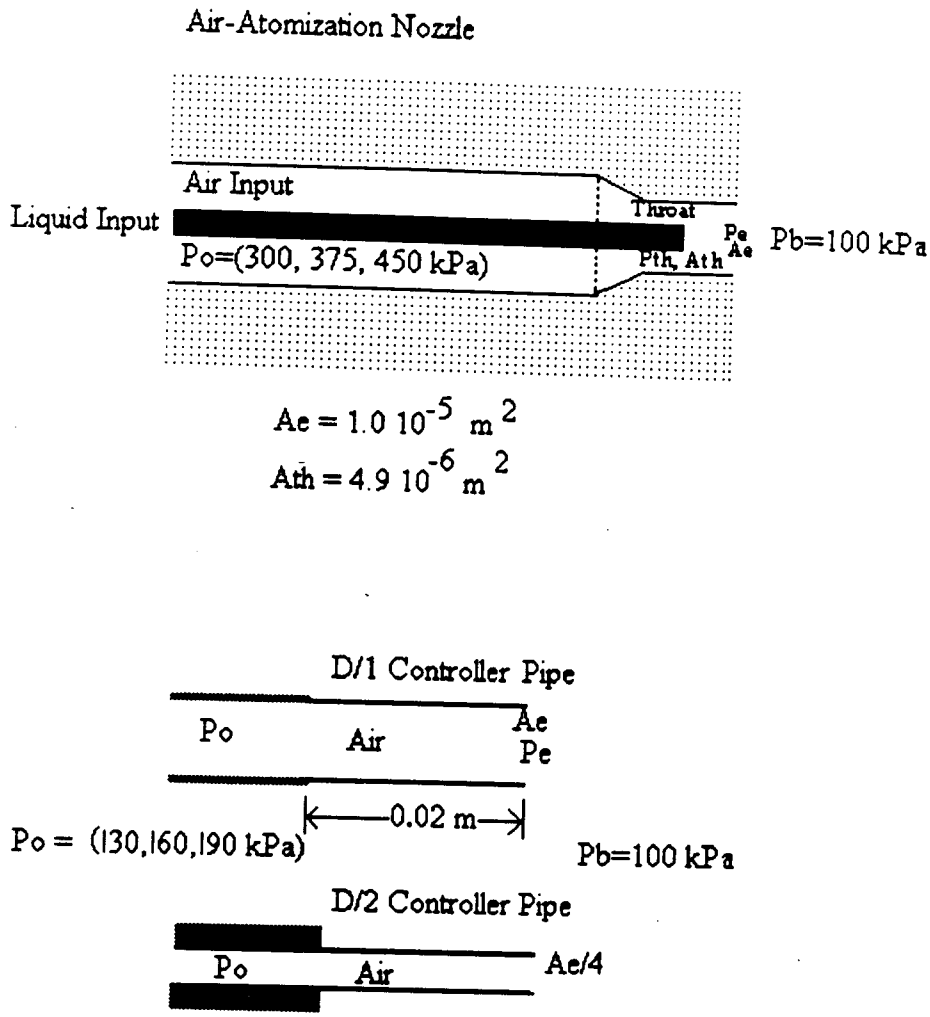

Figure 5. Nozzle and controller

The design pressure ratio follows from Equation 4, $\frac{p_o}{p_e} = 11.21$, or $P_{e,design}$ equal to 27, 34, and 40 kPa. Since the nozzle throat is clearly sonic by design, then the nozzle is choked at all three operating pressures and its mass flow rate is maximum and could be calculated from Equation 8 as 3.45, 4.32, and 5.18 g/s. These values are in good agreement with those discussed earlier indicating that the flow regime of the rotameter-nozzle system could be described by laws of the nozzle flow.

In order to determine the air pressures at the exit, we could (given the operating pressure ratios are considerably smaller than 0.528) assume the occurrence of a normal shock at the exit and assume the Mach number just upstream of the shock to remain equal to 2.23. Then, Equation 8 could be used (where P_2 is the exit pressure and P_1 is the throat design pressure) to calculate the pressures at the exit as 151, 187, and 227 kPa. All these values are considerably higher than the back pressure (100 kPa) indicating that the shock could have not occurred before the exit resulting in an exit supersonic flow with exit pressure equal to the back pressure. It follows that, at the exit, the nozzle flows at standard conditions. The exit air velocities and Reynolds numbers were calculated based on the equation of state and the standard conditions and are shown in Table 1.

Controller-Jet Pipe Flow. The controller pipe is shown in Figure 5. The figure shows the controller to have a regular geometry, steady operating pressures of 130, 160, and 190 kPa, a constant back pressure of 100 kPa, and a constant temperature of 295 ^{o}K. The back-to-operating pressure ratios as given by equation 7 are 0.769, 0.625, and 0.526. All ratios being higher than 0.528, indicate that the controller flow remains subsonic under the given operating pressures. No choking phenomena would take place and the mass flow rates would not reach maximum. At the exit, the flow is at standard conditions of pressure and density. Because of the very short length of the controller pipe (0.02 m), duct flow regime could not develop and the rotameter-controller system flow remains dominated by laws of the orifice flow of the rotameter. The controller-jet exit velocities and Reynolds numbers were calculated based on the equation of state at standard conditions and are shown in Table 1.

The exit velocities and the Reynolds numbers of the main-jet nozzle clearly indicate that the nozzle is supersonic and highly turbulent. The exit velocities and Reynolds numbers of the controller jet indicate that the controller jet flow is turbulent and subsonic. The D/2 controller operating at 190 kPa pressure, actually flows at sonic velocity in accordance with the back-to-operating pressure ratio (0.526) which fell under the sonic critical number 0.528. Table 1 indicates that even though the D/1 controller consumed twice as much air mass flow rate as the D/2 controller, it provided only half as much disturbing velocity magnitude. The counter

balance between exit velocity and exit diameter relative to different controller sizes, resulted into similar Reynolds numbers.

Total Air Mass and Power Input to the Nozzle-Controller System. The embodied power in compressed air is often a significant constraint in design of pneumatic systems. The power input into the nozzle-controller system was calculated for all operating pressures using an empirical technique commonly used in industry which is bounded by theoretical values for adiabatic and isothermal compression. A one-stage compressor case was assumed since it is the case most often used in such example of agricultural application

A summary of the calculations appears in Table 2. The D/1 controller required significant additional air mass. The D/2 controller required less mass; however, at higher pressures, it still considerably increased the air requirement. The power input into the controller could exceed the power input into the main jet. While the D/2 controller operated at higher pressures than the D/1 controller, the lower mass flow resulted in lower power requirements for the D/2 controller.

Velocity Decay along the Nozzle Assembly Centerline. Velocity measurements were interpreted according to a three-axis rectangular coordinate system consistent with Wygnanski and Fedler (1969). The x-axis was defined along the vertical laser beam with the origin at the nozzle exit pointing downward to the laboratory floor. The y-axis and the z-axis defined the horizontal plane perpendicular to the x-axis. The centerline velocity decay analysis was based on the following two-parameter exponential decay function developed by Abramovich (1963) and expressed as:

$$U_{cl} = U_r(\frac{x}{x_r})^{-b}, \qquad (9)$$

where: U_{cl} is the mean centerline air velocity in m/s, Ur is a reference centerline location air velocity in m/s, x is the distance from nozzle exit along the centerline in m, x_r is the distance from nozzle exit to the reference centerline location in m, and b is a dimensionless characteristic decay coefficient. Ur and x_r are normalizing factors for U and x respectively. The reference location could be any x location. Since velocity profiles were sampled at 0.30 m and at 0.60 m, downstream x-locations, x_r values of 0.30 m and 0.60 m were tried and resulted into equal b estimates and U fits. Since later spray deposition studies were done with setting the nozzle-to-plant canopy distance to 0.30 m, x_r was set to 0.30 m in order to provide a basis for comparison.

The practical aspect of this equation is that Ur gives an indication of controller effects, if any, on the flow field velocity magnitude and therefore the strength of the emitted jet, and b indicates the effects of the controller, if any, on the velocity decay of the emitted jet. According to the two-dimensional turbulent jet theory presented by Abramovich (1963), the centerline

Table 2. Total air mass and input power requirement to the nozzle-controller system.

Main Jet Gauge Pressure kPa	Controller Jet Gauge Pressure kPa	*Total Mass Flow Rate g/s	*Total Power Input W
		D/1 Controller	
	0	3.15	388
200	30	5.19	444
	60	6.47	568
	90	7.61	716
	0	4.42	611
275	30	6.46	667
	60	7.74	791
	90	8.88	939
350	0	5.76	917
	30	7.80	973
	60	9.08	1097
	90	10.22	1245
		D/2 Controller	
	0	3.15	388
	30	4.09	418
200	60	4.71	464
	90	5.27	552
	0	4.42	611
275	30	5.36	641
	60	5.98	687
	90	6.54	775
	0	5.76	917
350	30	6.70	947
	60	7.32	993
	90	7.88	1081

* Calculated as the sum of one nozzle jet and two controller jet requirements.

velocity of a circular jet was proportional to $x^{-1.0}$ and the centerline velocity of a plane jet was proportional to $x^{-0.50}$. Since the use of the controller was hypothesized to bound the geometry of the emitted jet by the circular and the plane jet geometry, it was hypothesized that the b parameter estimates would be bounded by 0.5 for the plane-shaped jet resulting from high disturbance and 1.0 for the undisturbed originally circular jet.

For each treatment combination of main jet pressure and controller pressure and diameter, values of Ur and b parameters were estimated by least-squares techniques and appear in Table 3. Because of the non-linearity of the model defined by equation 9, the R^2 values shown in the table

were obtained by correlating calculated velocity values with observed velocity values. The statistical results show that, for all treatment combinations, the correlation between estimated and observed values was high and the standard errors were low.

Table 3. Parameter estimates, standard errors and R^2 from least-square fit of Equation 9 to observed data of center line velocity decay at various main jet pressures and controller jet sizes and pressures.

Main jet pressure kPa	Controller jet pressure kPa	$U_{0.3}$ m/s	Standard error of $U_{0.3}$	b	Standard error of b	R^2
			Controller D/2			
	0	10.77	0.065	0.80	0.013	0.99
200	30	10.62	0.070	0.79	0.014	0.99
	60	7.35	0.098	0.64	0.027	0.97
	90	3.90	0.046	0.58	0.024	0.97
	0	13.55	0.122	0.85	0.020	0.99
275	30	13.36	0.091	0.82	0.015	0.99
	60	11.84	0.164	0.81	0.031	0.98
	90	7.76	0.142	0.61	0.037	0.94
	0	14.23	0.087	0.80	0.014	0.99
350	30	13.28	0.091	0.78	0.015	0.99
	60	11.43	0.141	0.82	0.027	0.99
	90	7.81	0.167	0.72	0.045	0.94
			Controller D/1			
	0	11.36	0.124	0.84	0.024	0.98
200	30	10.44	0.157	0.85	0.034	0.97
	60	6.93	0.151	1.07	0.054	0.96
	90	3.65	0.129	0.66	0.073	0.83
	0	14.02	0.122	0.90	0.020	0.99
275	30	13.29	0.114	0.85	0.019	0.99
	60	10.68	0.148	0.96	0.033	0.98
	90	5.73	0.224	1.19	0.103	0.91
350	0	14.46	0.174	0.79	0.026	0.98
	30	13.52	0.102	0.75	0.017	0.99
	60	11.58	0.141	0.71	0.026	0.98
	90	9.49	0.311	0.71	0.069	0.87

Estimates of Ur and b indicate a strong confirmation of the hypothesized gradual decrease of flow field velocity magnitude due to gradual increase of controller pressure. For example, at the 0.3 m downstream location, the velocity of the 200 kPa main jet of 10.77 m/s decayed to 7.35

m/s with the 60 kPa D/2 control pressure and decayed to 3.9 m/s with the 90 kPa D/2 control pressure. Under similar control conditions, the 275 kPa main jet had its velocity decayed from 13.55 m/s to 11.64 m/s and 7.76 m/s, respectively. The parameter estimates showed that for both controller sizes, the controller pressure of 30 kPa had very small effects of velocity magnitude reduction (Ur estimates) and pattern geometry alteration (b estimates). The 60 kPa controller pressure appeared to have produced moderate effects and the 90 kPa controller pressure appeared to have produced the strongest effects of velocity magnitude reduction. The b parameter estimates show a variation from values somewhat representative of a circular jet geometry (0.9 to 0.8) to values representative of a plane jet geometry (0.6 to 0.5) as the controller jet pressure increased. This indicates a strong confirmation of the hypothesis of jet geometry alteration, however, neither the undisturbed jet had perfect circular geometry, nor the maximum disturbance lead to perfect plane geometry. Overall, the D/2 controller appeared to have imposed smaller velocity magnitude reduction effects, but better and more consistent flow field geometry alteration effects than the D/1 controller as indicated by the gradual change of b estimates within the prescribed range from the 1.0 boundary towards the 0.5 boundary. The controller showed smoother action by acting on the 275 kPa main jet pressure. Relatively, the controller appeared to have inflicted stronger effects on the 200 kPa main jet pressure and weaker effects on the 350 kPa main jet pressure.

Shape of the Flow Field. Two-dimensional velocity profile data were taken at two downstream locations; x = 0.3 m and x = 0.6 m. Data were collected along a two-dimensional grid in the planes perpendicular to the x-axis. Both y and z dimensions varied from -0.12 to 0.12 m for the x = 0.3 m sampling station and from -0.16 to 0.16 m for the x = 0.6 m sampling station, because the flow field becomes wider further downstream. The controller jets were set parallel to the z dimension ; therefore, it was hypothesized that the controller would act to distort the main jet along the z dimension causing widening of the flow field along the y dimension. Contour plots of the mean velocity profile data for the 275 kPa main jet pressure, subject to different controller pressures and sizes at both downstream locations are shown in Figures 6-8. The plots show the uncontrolled jet to be circular in shape and, for all 3 main jet pressures, the 30 kPa controller pressure produced little effects of velocity magnitude reduction, but no effects of flow field shape distortion. The plots show that higher controller pressures produced noticeable effects of both velocity magnitude reduction and gradual flow field shape distortion from a circular geometry towards an elliptical geometry.

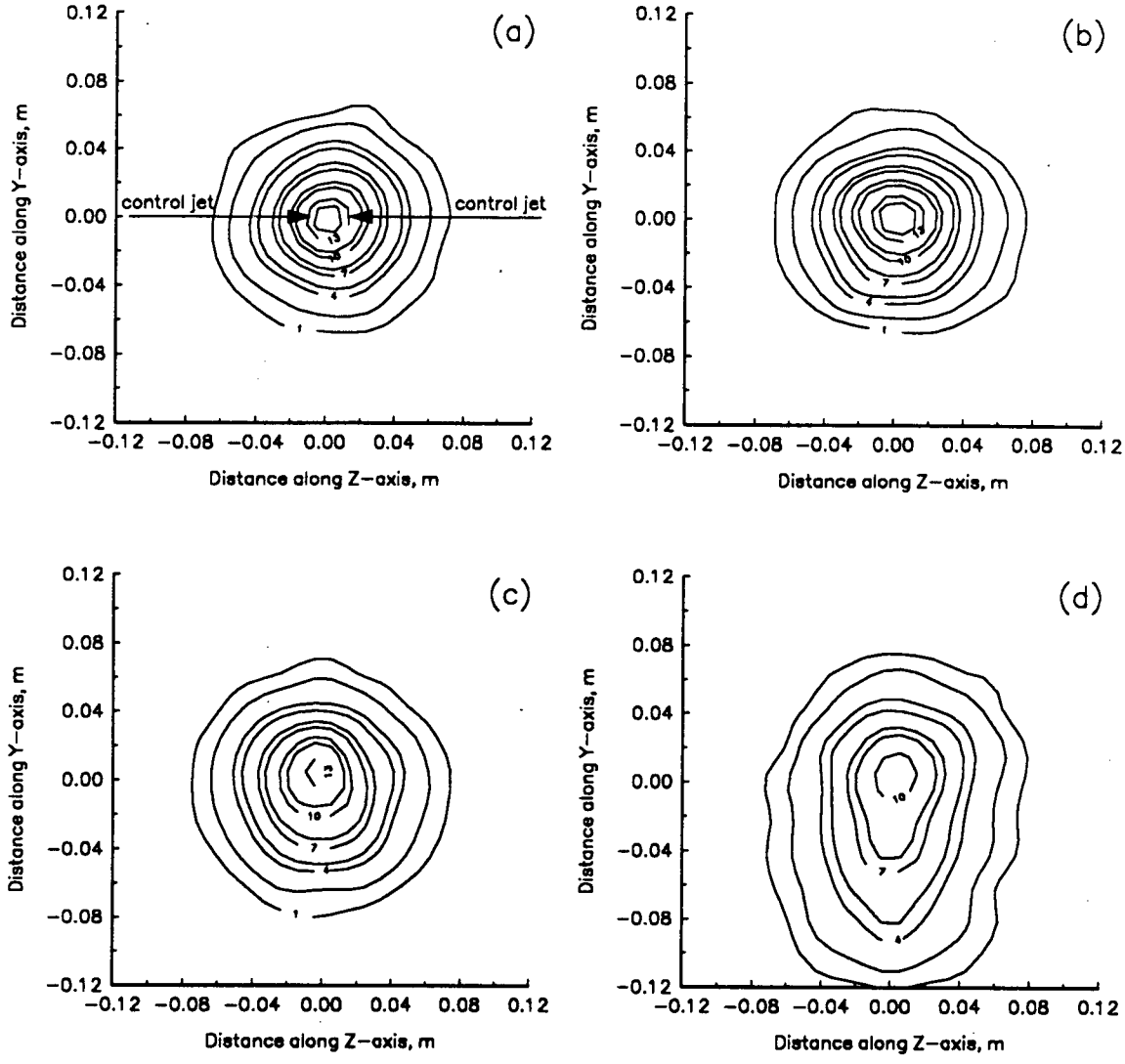

Figure 6. Contour plots (in m/s) of the observed mean velocity profiles indicating the flow field shape at 0.3 m downstream for main jet pressure 275 kPa and D/1 control pressures: (a) 0 kPa, (b) 30 kPa, (c) 60 kPa, and (d) 90 kPa.

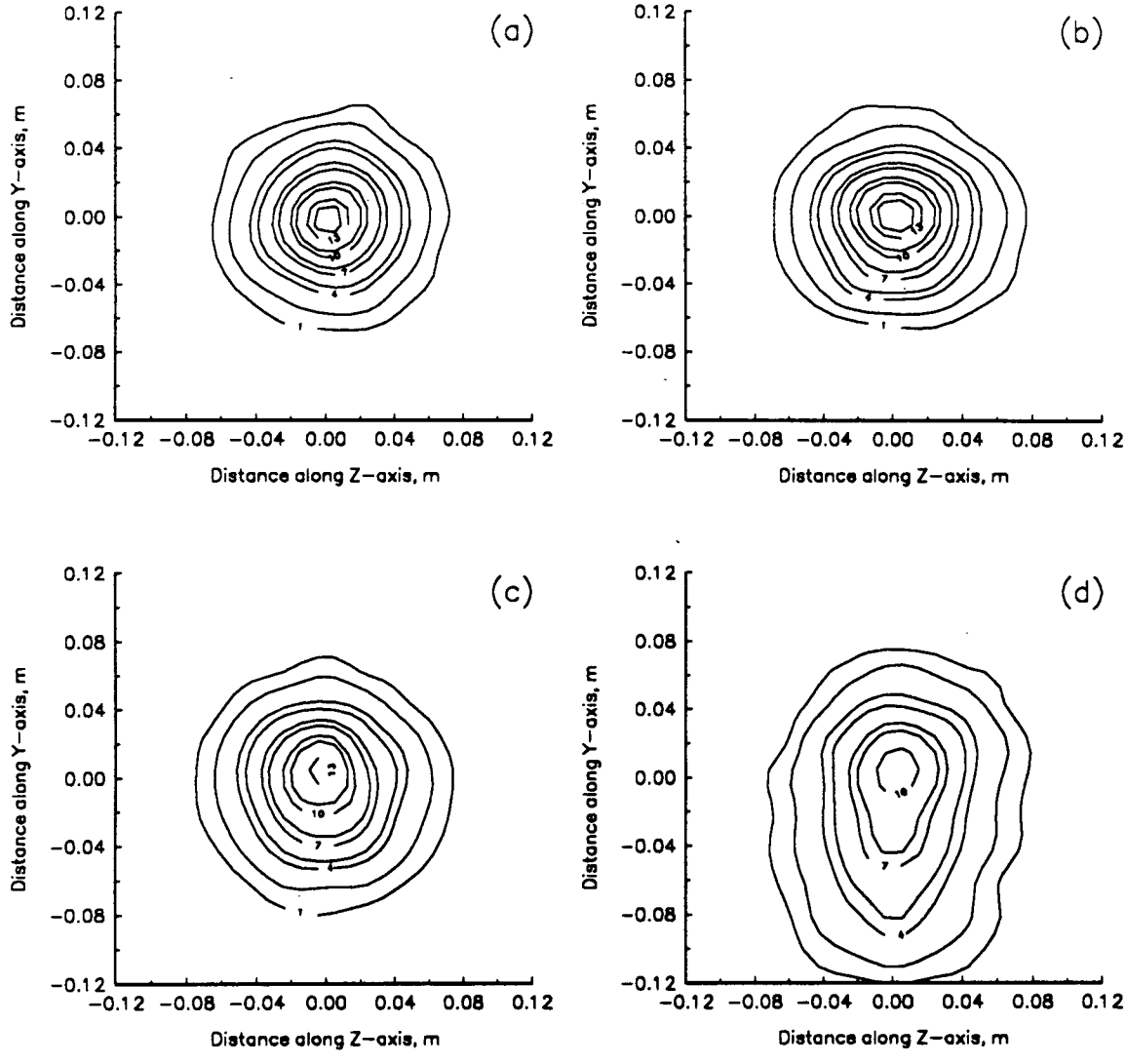

Figure 7. Contour plots (in m/s) of the observed mean velocity profiles indicating the flow field shape at 0.3 m downstream for main jet pressure 275 kPa and D/2 control pressures: (a) 0 kPa, (b) 30 kPa, (c) 60 kPa, and (d) 90 kPa.

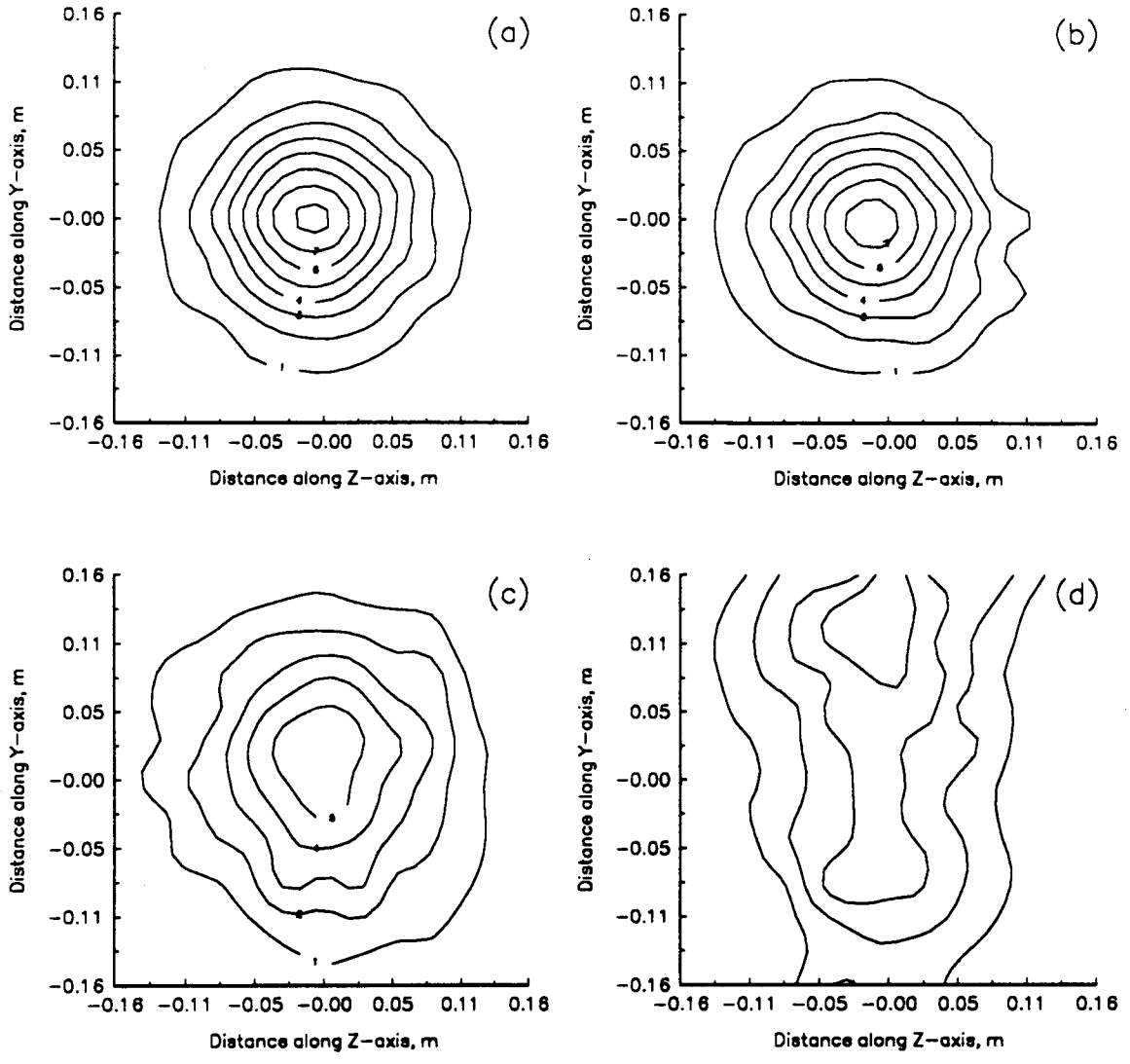

Figure 8. Contour plots (in m/s) of the observed mean velocity profiles indicating the flow field shape at 0.6 m downstream for main jet pressure 275 kPa and D/1 control pressures: (a) 0 kPa, (b) 30 kPa, (c) 60 kPa, and (d) 90 kPa.

Mean Local Velocity Profiles. A continuous, non-dimensional function for the velocity profiles of an axially symmetric circular jet was described by White (1974) as of the form:

$$\frac{U(r,x)}{U(0,x)} = (1+\frac{\Phi^2}{4})^{-2}, \qquad (10)$$

with $\Phi = \sigma_r \frac{r}{x_r}$,

where U(r, x) is the average velocity in m/s, U(r = 0, x) is the centerline average velocity at the location, x; r is the radial distance outward from jet centerline, obtained as $\sqrt{y^2+z^2}$, σ_r is a dimensionless constant, typically $5 < \sigma_r < 25$.

Giles et al. (1991) developed a two-dimensional model of equation 10 to describe velocity profiles of an axially similar elliptical jet produced by a dual-port air-atomization nozzle. Physically, the model represented expansion of an axially symmetric profile to an axially similar profile by forming the product of the non-dimensional profiles along y and z dimensions leading to the form:

$$\frac{U(y,z,x)}{U(0,0,x)} = (1+\frac{\Phi_y^2}{4})(1+\frac{\Phi_z^2}{4})^{-2}, \qquad (11)$$

with, $\Phi_y = \sigma_y \frac{y}{x}$, and $\Phi_z = \sigma_z \frac{z}{x}$,

where all variables are analogous in definition to equation 10. Both of the models defined by equations 10 and 11 were used for the analysis of observed velocity profiles produced by the nozzle-controller system jet. The hypothesis was that the radial model would provide an accurate description of velocity profiles of the uncontrolled, originally circular jet, and the two-dimensional model would provide an accurate description of velocity profiles of the controlled jet shown to have acquired an elliptical geometry. The use of both models set a basis for comparison and provided means of tracing the transition from circular to elliptical geometry due to gradual distortion of the flow field imposed by the controller action.

Equations 10 and 11 were fitted to the observed velocity profile data taken at x = 0.3 m and x = 0.6 m sampling locations. The fit was done using iterative, least-squares techniques. For fitting of equation 10, the radial distance, r, was calculated as the vector sum of y and z distances from the nozzle centerline. Prior to statistical analysis, the U(r = 0, x) and U(y = 0, z = 0, x) denominator terms on the left hand side of equations 10 and 11 were moved to the right hand side of the equations and were statistically estimated rather than being assigned values from observed data. Physically the terms corresponded to the centerline velocities of the flow field. The results of the statistical analysis appear in Tables 4 through 7. The R^2 values shown in the tables were obtained by correlating the calculated velocity values with the observed values. The undisturbed flow field appeared similarly well described by both of equations 10 and 11 as evidenced by the

relatively high correlation coefficients, the relatively consistently small standard errors of U and σ estimates (Tables) and the good fit of the calculated velocity profiles to the observed velocity profiles (plot (a) of the figures). The least-squares estimates of σ_r, and σ_y and σ_z ranged from 13.0 to 14.5 and from 12.0 to 13.5 respectively. All σ values were well positioned within the range of 5 to 25 and did not appear different with respect to main jet pressure nor with respect to dimension, however, little difference is noticeable with respect to sampling location. For the undisturbed flow field, the non-difference between σ_y and σ_z estimates indicates the similarity in width and shape of velocity profiles along y and z dimensions. The quality of σ_r, σ_y and σ_z estimates is well fulfilling to the expectations and confirms strongly the circularity and rules out ellipticity of the geometry of the undisturbed flow field. Comparison between σ estimates with respect to sampling location indicate that the estimates for the x = 0.6 m sampling location are consistently smaller than those for the x = 0.3 m sampling location supporting the intuitive notion that the flow field expands further downstream resulting in wider velocity profiles. The downstream expansion of the flow field is justified by equations 10 and 11; The smaller the σ value, the bigger gets the term $(1+\Phi^2/2)^{-2}$ and, therefore, the wider the profile becomes.

Considering the controller action imposed by each of the controller pressures and the flow field distortion hypothesis stating that the distortion occurs along the z dimension and the ellipticity adds along the y dimension, the statistical results for the 30 kPa controller pressure do not appear to have varied much from those relative to the undisturbed flow field indicating no noticeable effects on the geometry of the flow field. However, estimates for the 200 kPa main jet pressure and the D/1 case appear to have varied from those for the same undisturbed case. The radial model appears to have lost ability to describe the flow field geometry as evidenced by the relative reduction of the correlation coefficient. The two-dimensional model showed noticeable reduction of σ_y estimates only indicating a start of velocity profile widening along the y dimension. Overall, the 30 kPa controller pressure effect may be described as a stage of transitional, dimensionally undetermined, distortion of the flow field. The statistical results for the 60 and 90 kPa controller pressures appear to have varied much from those relative to the undisturbed flow field. The local mean velocities have reduced significantly relative to the main jet pressure, the controller size and pressure, and the sampling location.

Table 4. Parameter estimates, standard errors and R^2 from fit of Equations 10 and 11 to observed data of flow field velocity at location of 0.3 m and controller size D/2 at various main jet and controller jet pressures

		Radial expression				
Main jet pressure kPa	Controller jet pressure	σ_r	Standard error of σ_r	$U_{0.3}$ m/s	Standard error of $U_{0.3}$	R^2
	0	13.46	0.154	13.09	0.188	0.97
200	30	12.66	0.146	12.79	0.184	0.96
	60	9.13	0.224	8.52	0.250	0.83
	90	5.82	0.318	4.45	0.250	0.40
	0	13.61	0.245	16.13	0.364	0.91
275	30	13.21	0.114	16.19	0.174	0.98
	60	10.66	0.325	11.98	0.449	0.77
	90	8.37	0.232	9.41	0.305	0.79
	0	12.93	0.125	18.51	0.223	0.97
350	30	12.46	0.142	17.19	0.244	0.96
	60	12.20	0.146	15.99	0.238	0.96
	90	11.10	0.174	13.10	0.253	0.93

		Two-dimensional expression						
Main jet pressure kPa	Controller jet pressure kPa	σ_v	Standard error of σ_v	σ_z	Standard error of σ_z	$U_{0.3}$ m/s	Standard error of $U_{0.3}$	R^2
	0	12.56	0.183	12.26	0.179	12.59	0.167	0.97
200	30	12.08	0.177	11.30	0.167	12.31	0.165	0.97
	60	7.30	0.226	9.90	0.284	8.33	0.216	0.85
	90	2.90	0.249	9.21	0.393	4.78	0.184	0.65
	0	13.51	0.302	11.78	0.269	15.62	0.323	0.92
275	30	12.75	0.130	11.66	0.120	15.57	0.146	0.98
	60	8.84	0.347	10.98	0.415	11.60	0.399	0.79
	90	5.81	0.169	10.52	0.256	9.50	0.211	0.88
	0	12.05	0.146	11.79	0.143	17.79	0.197	0.98
350	30	11.70	0.168	11.28	0.163	16.56	0.216	0.97
	60	11.44	0.173	11.08	0.168	15.38	0.212	0.96
	90	10.24	0.205	10.26	0.206	12.60	0.227	0.94

Table 5. Parameter estimates, standard errors and R^2 from fit of Equations 10 and 11 to observed data of flow field velocity at location of 0.3 m and controller size D/1 at various main jet and controller jet pressures.

		Radial expression				
Main jet pressure kPa	Controller jet pressure	σ_r	Standard error of σ_r	$U_{0.3}$ m/s	Standard error of $U_{0.3}$	R^2
	0	13.27	0.160	12.66	0.191	0.96
200	30	11.84	0.208	10.89	0.237	0.92
	60	8.11	0.313	6.76	0.303	0.65
	90	6.00	0.361	4.09	0.257	0.34
	0	13.52	0.185	15.20	0.261	0.95
275	30	13.01	0.154	14.76	0.218	0.96
	60	10.61	0.191	11.82	0.260	0.91
	90	6.61	0.332	6.15	0.336	0.49
	0	13.00	0.173	16.93	0.281	0.95
350	30	12.31	0.157	16.61	0.264	0.96
	60	11.78	0.166	15.42	0.269	0.95
	90	11.26	0.239	12.55	0.328	0.88

		Two-dimensional expression						
Main jet pressure kPa	Controller jet pressure kPa	σ_v	Standard error of σ_v	σ_z	Standard error of σ_z	$U_{0.3}$ m/s	Standard error of $U_{0.3}$	R^2
	0	12.44	0.193	12.06	0.188	12.18	0.173	0.96
200	30	10.94	0.249	10.92	0.248	10.48	0.216	0.92
	60	5.95	0.300	9.51	0.411	6.68	0.261	0.70
	90	2.53	0.318	8.92	0.477	4.04	0.194	0.52
	0	12.65	0.223	12.31	0.218	14.62	0.236	0.95
275	30	12.38	0.183	11.64	0.173	14.21	0.192	0.96
	60	9.05	0.207	10.59	0.236	11.39	0.230	0.91
	90	4.30	0.304	8.79	0.447	6.28	0.285	0.58
	0	12.16	0.207	11.82	0.202	16.28	0.253	0.95
350	30	11.40	0.185	11.33	0.184	15.97	0.235	0.96
	60	11.25	0.199	10.49	0.187	14.84	0.239	0.95
	90	10.35	0.283	10.48	0.298	12.08	0.298	0.88

Table 6. Parameter estimates, standard errors and R^2 from fit of Equations 10 and 11 to observed data of flow field velocity at location of 0.6 m and controller size D/2 at various main jet and controller jet pressures.

Radial expression

Main jet pressure kPa	Controller jet pressure	σ_r	Standard error of σ_r	$U_{0.6}$ m/s	Standard error of $U_{0.6}$	R^2
200	0	13.65	0.243	6.58	0.112	0.93
	30	13.35	0.185	6.79	0.090	0.95
	60	10.98	0.148	5.29	0.067	0.95
	90	6.16	0.309	2.67	0.108	0.40
275	0	14.05	0.143	8.60	0.084	0.98
	30	13.84	0.109	8.59	0.065	0.99
	60	12.97	0.142	7.80	0.082	0.97
	90	9.79	0.239	5.61	0.128	0.83
350	0	13.29	0.201	9.58	0.138	0.95
	30	13.22	0.131	9.39	0.089	0.98
	60	12.42	0.308	8.04	0.189	0.86
	90	11.70	0.320	6.83	0.177	0.82

Two-dimensional expression

Main jet pressure kPa	Controller jet pressure kPa	σ_v	Standard error of σ_v	σ_z	Standard error of σ_z	U0.6 m/s	Standard error of U0.6	R^2
200	0	12.83	0.303	12.97	0.307	6.44	0.106	0.93
	30	12.69	0.235	12.58	0.232	6.66	0.085	0.96
	60	9.76	0.166	11.17	0.190	5.21	0.061	0.95
	90	3.19	0.326	9.57	0.411	2.79	0.086	0.62
275	0	13.24	0.175	13.30	0.176	8.43	0.078	0.98
	30	13.31	0.134	12.84	0.129	8.41	0.059	0.98
	60	12.64	0.181	12.07	0.174	7.64	0.077	0.97
	90	7.96	0.243	11.02	0.327	5.59	0.113	0.85
350	0	12.93	0.257	12.20	0.241	9.38	0.129	0.95
	30	12.45	0.160	12.55	0.161	9.20	0.082	0.98
	60	11.84	0.387	11.67	0.381	7.89	0.381	0.86
	90	10.80	0.392	11.36	0.414	6.70	0.168	0.82

Table 7. Parameter estimates, standard errors and R^2 from fit of equations 10 and 11 to observed data of flow field velocity at location of 0.6 m and controller size D/1 at various main jet and controller jet pressures.

Radial expression

Main jet pressure kPa	Controller jet pressure	σ_r	Standard error of σ_r	$U_{0.6}$ m/s	Standard error of $U_{0.6}$	R^2
200	0	13.69	0.243	6.85	0.117	0.93
	30	10.97	0.368	5.05	0.160	0.73
	60	8.25	0.267	4.02	0.118	0.68
	90	3.88	0.393	1.76	0.097	0.10
275	0	13.58	0.171	8.36	0.101	0.96
	30	13.67	0.177	8.21	0.102	0.96
	60	10.98	0.195	6.4	0.111	0.91
	90	6.75	0.286	3.95	0.141	0.50
350	0	13.64	0.164	9.63	0.111	0.97
	30	13.23	0.136	9.51	0.093	0.98
	60	12.74	0.223	8.53	0.142	0.93
	90	10.03	0.436	5.32	0.216	0.61

Two-dimensional expression

Main jet pressure kPa	Controller jet pressure kPa	σ_v	Standard error of σ_v	σ_z	Standard error of σ_z	$U_{0.6}$ m/s	Standard error of $U_{0.6}$	R^2
200	0	13.39	0.312	12.76	0.302	6.71	0.111	0.93
	30	9.14	0.405	11.52	0.509	4.93	0.509	0.74
	60	5.77	0.240	10.56	0.363	4.06	0.097	0.78
	90	0.15	3.744	0.59	0.488	1.77	0.089	0.26
275	0	12.89	0.212	12.79	0.211	8.19	0.094	0.96
	30	13.20	0.227	12.66	0.217	8.05	0.096	0.96
	60	10.09	0.239	10.74	0.255	6.52	0.106	0.91
	90	3.73	0.256	10.41	0.373	4.13	0.105	0.72
350	0	12.97	0.205	12.81	0.202	9.43	0.104	0.97
	30	12.42	0.165	12.60	0.168	9.32	0.086	0.98
	60	11.95	0.278	12.14	0.283	8.35	0.135	0.93
	90	8.46	0.490	10.73	0.611	5.26	0.205	0.62

Compared to the undisturbed case, the σ_r estimates have dropped significantly and relatively to treatment cases. Overall, the D/1 controller imposed more reduction than the D/2 controller. The drop in σ_r estimates could indicate that velocity profiles have become wider because they still are well positioned within the expected range of 5 to 25, but the relatively significant reduction in correlation coefficients and increase in standard errors (tables) and the poor fit of the model to the observed data (bottom plots of all figures) indicate that the radial model no longer describes the flow field. The behavior of the radial model parameter estimates has identified the distortion of the flow field, but could not dimensionally describe it.

Compared with the undisturbed case, the σ_y and σ_z estimates have also significantly decreased. The reduction of σ_y estimates appears consistently and significantly higher than that of σ_z estimates indicating that the velocity profiles have undergone significantly more widening along the y dimension. The σ_z estimates have undergone relatively small reductions, but have never increased in value indicating that the velocity profiles along the z dimension gained a little but never lost width. This means that the controller acted to add ellipticity along the y dimension but did not actually squeeze the flow field along the z dimension.

One may notice, especially for the 90 kPa controller pressure, that there is a tendency of the predicted y dimension profiles to flatten in response to width increase and the predicted z dimension profiles to maintain their bell shape in response to the controller action. This ability to adopt the shape of the distorted flow field, enables the two-dimensional model to describe the distortion phenomenon and support the distortion hypothesis. Compared to the D/2 controller which tended to preserve the integrity of the flow field structure, the D/1 controller acted stronger to disperse the flow field; some times up to a damaging level of its structure. For example, the D/1 controller pressure of 90 kPa severely dispersed the flow field of the 200 kPa main jet pressure at the 0.6 m downstream location ($\sigma_y = 0.15$ (s.e. = 3.74), $\sigma_z = 0.59$ (s.e. = 0.5), Ur = 1.77 and $R^2 = 0.26$). Overall, the controller effects were stronger on low and moderate main jet pressures and the controller was shown to be effective at both downstream locations.

Mass and Momentum of the Controlled Air Jet. Previous studies of the flow field of circular jets have demonstrated the conservation of momentum, but not the mass of such flows [Rajaratnam (1976)]. For a theoretically circular geometry air jet with centerline velocity inversely proportional to the downstream distance, Ricou and Spalding (1961) reported that, due to air entrainment, the mass flow increased proportionally with downstream distance. Giles et al. (1991) reported that the mass flow from a dual-port air-atomization nozzle increased proportionally to $x^{1.14}$ indicating that an axially similar dual-port jet entrained more ambient air than an axially symmetric jet. The flow field momentum, however, was inferred to have been conserved. In this study, the flow rates of mass and momentum characteristics of the controlled jet flow field were considered by evaluating the effects of the controller on air entrainment and

checking the status of momentum conservation. Mass and momentum calculations are based on the two-dimensional model represented by Equation 11 because this model proved to be more descriptive of the disturbed flow field than the radial model.

Equation 11 can be integrated over y and z from - ∞ to + ∞ to derive the mass flow rate equation as:

$$Q(x) = \pi^2 \rho U(y=0, z=0, x)(\frac{x^2}{\sigma_y \sigma_z}), \tag{12}$$

where ρ is the air density at standard conditions equal to 1200 g/m^3. Equation 8 representing the bulk centerline velocity was substituted for U(y=0, z=0, x) and the result was:

$$Q(x) = \frac{\pi^2 \rho U_{ref} x_{ref}^b}{\sigma_y \sigma_z} x^{2-b}, \tag{13}$$

It was noted that the reference location represented by Ur and xr did not, affect the centerline velocity estimates. Profile results showed little variation in σ estimates with respect to downstream location. By assuming no reference location effects on b, σy and σz, Ur and xr could arbitrarily be fixed and Equation 13 taken to represent the whole flow field. Equation 13 can be rearranged as:

$$Q(x) = K(b, \sigma y, \sigma z)\, x^{C(b)}, \tag{14}$$

and comparison between the different levels of control would be based on the values of K and C, since the values of b, σy and σz are dependent on controller levels only. Table 8 shows values of K and C for various main jet préssures subject to various levels of controller. The reference downstream location x=0.3 m was used. The table shows that K and C values appear to gradually increase in response to increasing controller levels indicating gradual increase of total air mass flow rate, especially for low and moderate main jet pressures. While the variation of K values could be attributed to the extra mass flow added by the controller jets and to the air entrainment, the variation of the C values is solely attributed to air entrainment. The D/2 controller appears to have a stronger and more steady trend of contribution to air entrainment as evidenced by the greater variation of its corresponding K and C values. K values relative to both controller sizes appear less explanatory of the high main jet pressure flow field.

Velocity profiles expressed by Equation 11 could further be manipulated to yield an expression for momentum rate of the controlled jet flow field (Giles, et.al., 1991). Integration of the square of Equation 11 over y an z = - ∞ to + ∞ resulted in:

$$M(x) = \frac{25}{64} \pi^2 \rho U(y=0, z=0, x)(\frac{x^2}{\sigma_y \sigma_z}), \tag{15}$$

Substitution of Equation 8 for U(y=0,z=0,x) and rearrangement of Equation 15 results in:

$$M(x) = \frac{25\pi^2 \rho (U_r x_r^b)^2}{64\sigma_y \sigma_z} x^{2(1-b)}, \tag{16}$$

Equation 16 could be evaluated for different treatment cases and compared at different downstream locations. The results could provide a possible check of momentum conservation with respect to flow field downstream location. By choosing an x-location equal to a reference location, Equation 16 yields

$$M(x_r) = \frac{25\pi^2 \rho}{64\sigma_y \sigma_z} (U_r x_r)^2, \tag{17}$$

all the variables for Equation 17 have already been estimated for downstream locations x = 0.3 m and x = 0.6 m. Momentum rate calculations at both locations are shown in Tables 9 and 10. Comparison, between locations, of the momentum rate values appearing in the last column of both tables show an agreement between downstream locations within 3 % for the D/2 controller and within 10 % for the D/1 controller. The variation of momentum rate values in response to controller levels supported the previous observations namely that the different controller levels produced different jet structures.

Table 8. Mass flow rate parameters K and C for various main jet pressures subject to various controller sizes and pressures

Main Jet Pressure kPa	Control Jet Press. kPa	Ur m/s	b	σy	σz	K	C
				D/2 Controller			
	0	10.77	0.80	12.56	12.26	316.16	1.20
200	30	10.62	0.79	12.08	11.30	355.95	1.21
	60	7.35	0.64	7.30	9.90	557.40	1.36
	90	3.90	0.58	2.90	9.21	860.24	1.42
	0	13.55	0.85	13.51	11.78	362.39	1.15
275	30	13.36	0.82	12.75	11.66	396.57	1.18
	60	11.84	0.81	8.84	10.98	544.81	1.19
	90	7.76	0.61	5.81	10.52	721.43	1.39
	0	14.23	0.80	12.05	11.79	452.77	1.20
350	30	13.28	0.78	11.70	11.28	465.95	1.22
	60	11.43	0.82	11.44	11.08	397.92	1.18
	90	7.81	0.72	10.24	10.26	370.00	1.28
				D/1 Controller			
	0	11.36	0.84	12.44	12.06	326.19	1.16
200	30	10.44	0.85	10.94	10.92	371.96	1.15
	60	6.93	1.07	5.95	9.51	399.98	0.93
	90	3.65	0.66	2.53	8.92	865.34	1.34
	0	14.02	0.90	12.65	12.31	360.81	1.10
275	30	13.29	0.85	12.38	11.64	392.54	1.15
	60	10.68	0.96	9.05	10.59	415.47	1.04
	90	5.73	1.19	4.30	8.79	428.50	0.81
	0	14.46	0.79	12.16	11.82	460.28	1.21
350	30	13.52	0.75	11.40	11.33	502.53	1.25
	60	11.58	0.71	11.25	10.49	494.33	1.29
	90	9.49	0.71	10.35	10.48	440.76	1.29

Table 9. Momentum rates for various main jet pressures subject to various controller sizes and pressures at x=0.3 m downstream location.

Main jet pressure kPa	Controller jet pressure kPa	σy	σz	$U_{0.3}$ m/s	$M_{0.3}$ gm^2/s
			D/2 controller		
	0	12.56	12.26	12.59	428.60
200	30	12.08	11.30	12.31	462.28
	60	7.30	9.90	8.33	399.77
	90	2.90	9.21	4.78	356.19
	0	13.51	11.78	15.62	638.33
275	30	12.75	11.66	15.57	678.97
	60	8.84	10.98	11.60	577.22
	90	5.81	10.52	9.50	614.81
	0	12.05	11.79	17.79	927.54
350	30	11.70	11.28	16.56	865.19
	60	11.44	11.08	15.38	777.02
	90	10.24	10.26	12.60	629.18
			D/1 controller		
	0	12.44	12.06	12.18	411.73
200	30	10.94	10.92	10.48	382.80
	60	5.95	9.51	6.68	328.35
	90	2.53	8.92	4.04	301.13
	0	12.65	12.31	14.62	571.52
275	30	12.38	11.64	14.21	589.44
	60	9.05	10.59	11.39	563.62
	90	4.30	8.79	6.28	434.46
	0	12.16	11.82	16.28	767.79
350	30	11.40	11.33	15.97	822.16
	60	11.25	10.49	14.84	777.00
	90	10.35	10.48	12.08	560.16

Table 10. Momentum rates for various main jet pressures subject to various controller sizes and pressures at x=0.6 m downstream location.

Main jet pressure kPa	Controller jet pressure kPa	σy	σz	$U_{0.6}$ m/s	$M_{0.6}$ gm^2/s
			D/2 controller		
	0	12.83	12.97	6.44	415.10
200	30	12.69	12.58	6.66	462.75
	60	9.76	11.17	5.21	414.68
	90	3.19	9.57	2.79	424.67
	0	13.24	13.30	8.43	672.14
275	30	13.31	12.84	8.41	689.27
	60	12.64	12.07	7.64	637.20
	90	7.96	11.02	5.59	593.30
	0	12.93	12.20	9.38	928.95
350	30	12.45	12.55	9.20	902.21
	60	11.84	11.67	7.89	750.37
	90	10.80	11.36	6.70	609.38
			D/1 controller		
	0	13.39	12.76	6.71	438.89
200	30	9.14	11.52	4.93	384.45
	60	5.77	10.56	4.06	450.56
	90	0.15	0.59	1.77	-
	0	12.89	12.79	8.19	677.62
275	30	13.20	12.66	8.05	645.84
	60	10.09	10.74	6.52	653.35
	90	3.73	10.41	4.13	731.62
	0	12.97	12.81	9.43	891.41
350	30	12.42	12.60	9.32	924.45
	60	11.95	12.14	8.35	800.44
	90	8.46	10.73	5.26	507.63

Conclusions from Stationary Field Studies. The flow field analysis of the stationary jet has demonstrated the effectiveness of the controller device for control of the velocity and shape of the air-jet emitted from the air-atomization nozzle. In the region of 0.1 to 0.6 m downstream of the nozzle exit, controller air supply pressure could be used to control jet velocity over a 2- to 4 fold turndown ratio. Similarly, the controller could double to triple the planar area covered by the jet flow. The following conclusions were drawn from the study:

1) A confirmation of the hypothesized gradual decrease of flow field velocity magnitude due to gradual increase of controller pressure.

2) A confirmation of the hypothesized gradual flow field shape distortion from a circular geometry towards an elliptical geometry.

3) The controller showed more usefulness by acting at moderate controller pressures on moderate main jet pressures. The controller appeared to have inflicted stronger effects on the lower main jet pressure and weaker effects on the larger main jet pressure.

4) The D/2 controller appeared to be less effective for control of velocity magnitude, but more effective for flow field geometry alteration than the D/1 controller.

5) The controller effects propagated downstream in the flow field.

6) The creation of turbulence appeared relative to the controller pressure and size and subject to the strength of the main jet. The D/1 controller appeared evenly effective on all main jet pressures, but the D/2 controller appeared more effective on lower main jet pressures.

7) The controller increased the proportion of ambient air entrained into the flow field of the air jet as the controller flow rates increased.

8) Different levels of control resulted into different jet structures, but within a single flow field structure, momentum rates showed an agreement between both downstream locations within 3 % for the D/2 controller and within 10 % for the D/1 controller.

9) While the controller could effectively control the main jet flow, it required significant air mass and power input. At high levels of control, controller power requirements approached those of the main jet. The small controller provided smoother control and required significantly less air mass and power input than the large controller.

Moving jet analysis. In the static jet analysis, the flow field produced by the nozzle-controller system was investigated and the effects of control on were characterized. In practice, the jet produced by an agricultural chemical spray nozzle is not stationary since the spray equipment travels along the crop. The nozzle-controller system, the air supply and monitoring, the anemometer system for air velocity measurement, and the hot-wire probe positioning system were part of the same experimental apparatus described earlier. The nozzle-controller system was attached to a carriage sprayer simulator with adjustable travel speed (0 to 2 m/s). Two dual-wire x-probes were used and each probe occupied two of the four channels of the anemometer-bridge

system. The use of a dual-wire probe provided measurement of both vertical and horizontal air jet velocity components. An overall view of the experimental setup is shown in Figure 9.

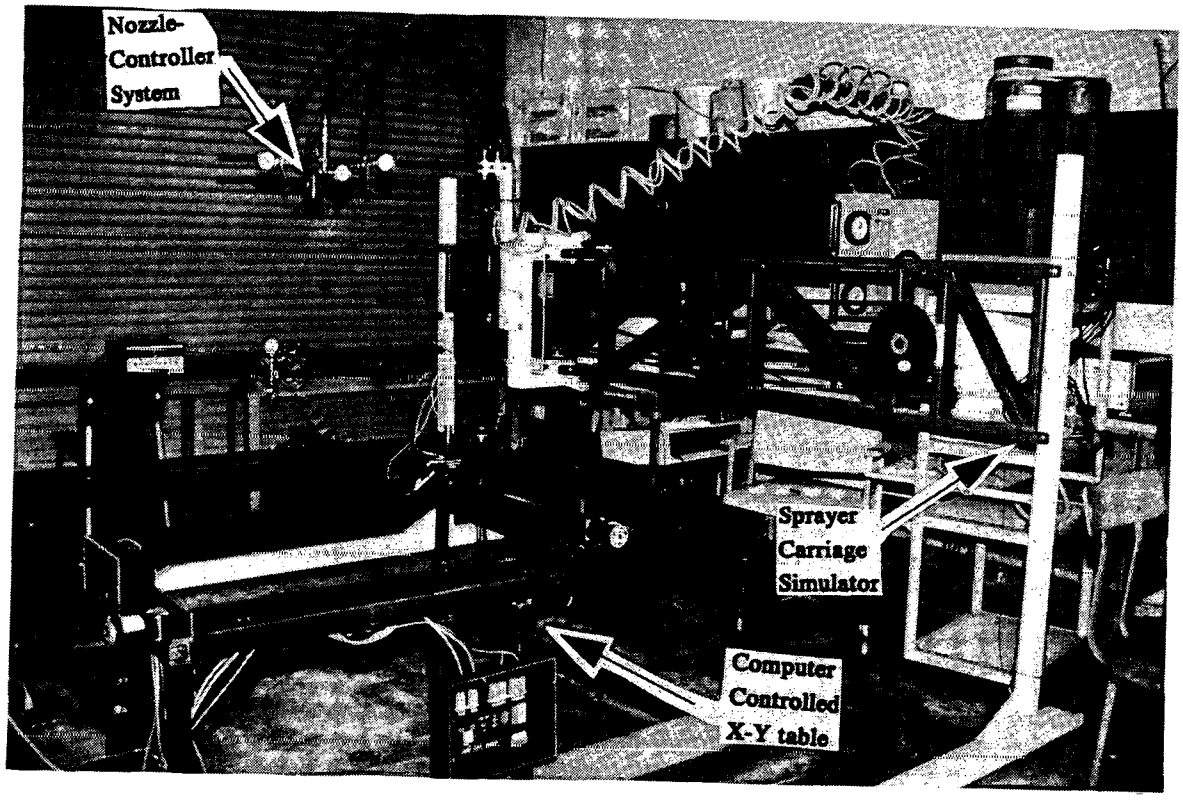

Figure 9. Experimental setup for moving jet study

The nozzle-controller system was positioned 2.5 m above the laboratory floor. The sprayer carriage simulator was operated at 1.5 m/s in single pass mode. This speed of about 5.4 km/h is a common tractor speed for spray application. The probes were positioned to simultaneously take air velocity measurements of the flow field at two vertical sampling locations. One probe was set at 0.3 m downstream from the nozzle exit and the other probe was set another 0.3 m further downstream directly under the first one. Probe supports were held in vertical position by means of a probe support holder as shown in Figure 10. Horizontally, the probes were positioned in the flow field at 0.02 m intervals along a 0.32 m path perpendicular to the nozzle travel path by means of the computer controlled positioner. The data acquisition card was set to sample for 1 second at a 4 kHz sampling rate. The proximity switch was positioned 0.2 m ahead of the air velocity sensor location. This offset provided an early triggering of the data acquisition card and allowed the reading of air velocities from the leading jet shoulder. Having realized the enormous time and resources requirement of the full experimental design setup for the stationary jet analysis, it was decided to allocate time and resources to fewer treatments which would include variation due to controller effects and comparison of effects with respect to total air mass and power input requirement. For the controller effect evaluation, the middle main-jet nozzle pressure of 275 kPa was shown in the previous section to provide insight into moderate controller effects. It was, therefore, selected and was subject to all four controller-jet pressures; 0, 30, 60, and 90 kPa and both the D/1 and the D/2 controller sizes. This combination defined seven treatments. Four additional treatments were selected to account for the comparison of effects based on the total air mass and power input requirement of the treatments. Two treatments were defined by the combination of 200 kPa main-jet and 90 kPa D/1 and D/2 controller-jet pressures, they had similar total air mass and power input requirement as the 275 kPa main-jet and (D/2) 30 kPa or (D/1) 60 kPa control jet pressures. The two other treatments were defined by the combination of 350 kPa main-jet and D/1 and D/2 60 kPa control jet pressures. They had similar total air mass and power input requirement as the treatment combination of 275 kPa main-jet and 90 kPa control jet pressures.

Analysis and Discussion of Moving Jet Study. Given the carriage speed of 1.5 m/s and the sampling period of 1 s, velocity measurements were taken along 1.5 m of the nozzle travel axis, that, is 0.2 m before the nozzle vertical center line coincided with the vertical plane defined by the two sampling probes, and 1.3 m after the nozzle passed by the probes. Given the sampling frequency, air velocities were sampled every 1/4000 of a second or every 0.375 mm. The data were smoothed by averaging out every 10 data points reducing the sample size to only 400.

The processing procedure resulted in event signatures of the moving jet at each horizontal sampling station across the nozzle travel axis. The shape of the flow field was characterized by creating a contour plot of all the signatures. The vertical component of the velocity was used.

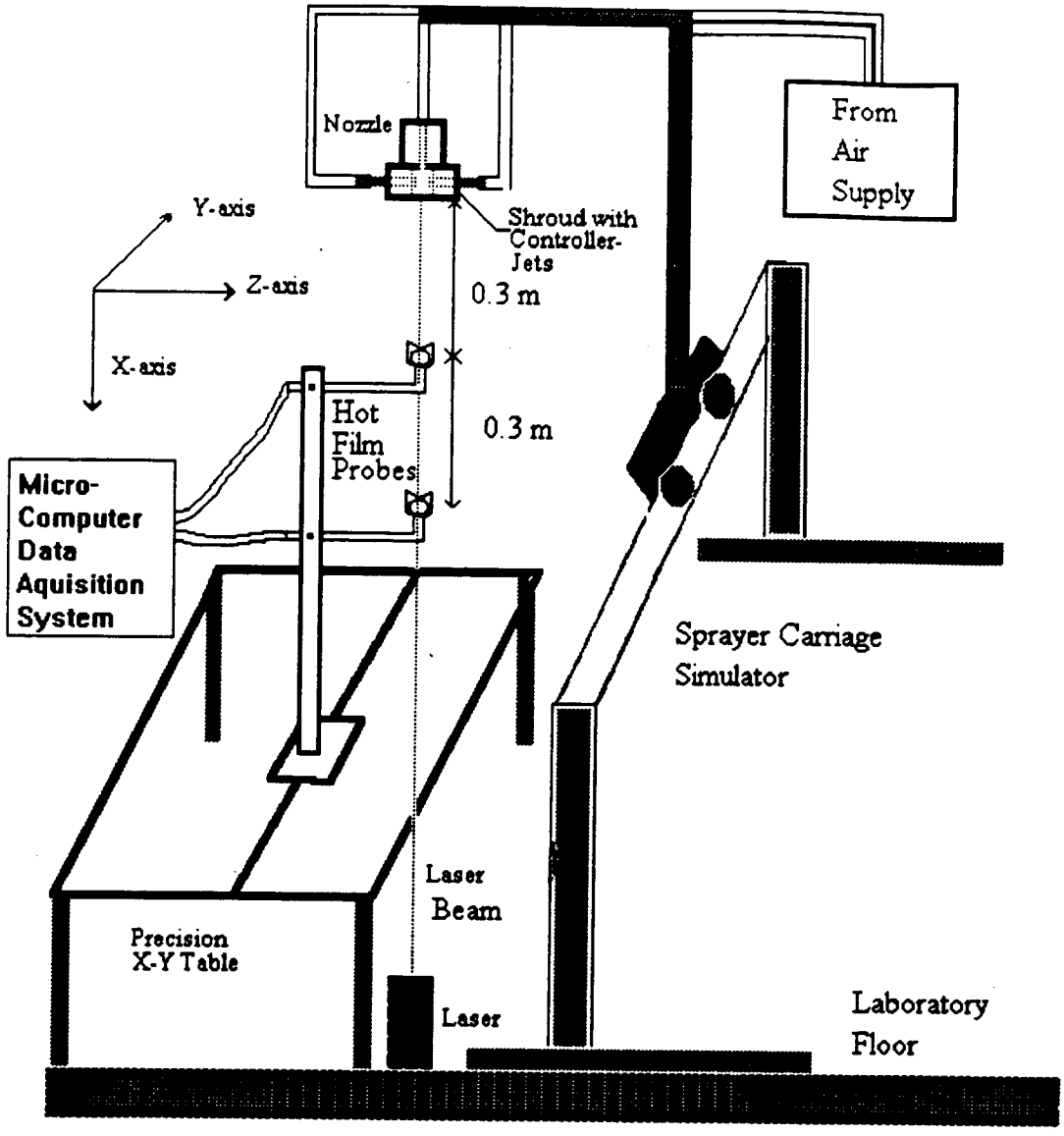

Figure 10. Probe setup for moving jet study

Flow field shapes were developed for both 0.3 m and 0.6 m vertical sampling stations and for all the treatments. The flow field shape plots could be interpreted as an instantaneous snap shot of the moving jet. Contour plots representative of the controller effect treatments are displayed in Figures 11 through 14. A close examination of the entire data set revealed: 1) The aerodynamic drag forces reshaped the geometry of the originally circular non controlled (0 kPa controller pressure) jet. At the upper location, the jet had acquired the shape of a comet or a distorted ellipse. The kidney shape described by Abramovich (1963) was more apparent at the lower station. 2) The aerodynamic drag forces deflected the jet backward, opposite to its travel direction. At the upper station, the leading shoulder of the non controlled jet, which at stationary status, stretched along 0.12 m around the nozzle center line, stretched only about 0.02 m forward and about 0.26 m backward from the nozzle center line axis. The leading edge of the moving jet was deflected about 0.1 m backward and the trailing edge was deflected about 0.14 m backward. The central core of the jet, represented by air velocities greater than 4 m/s, was not deflected as much deflection as the periphery of the jet represented by air velocities less than 2 m/s. At the lower sampling station, the leading shoulder of the non controlled jet, which at stationary status stretched along 0.16 m around the nozzle center line, tailed about 0.04 m behind. The trailing edge tailed more than 0.5 m behind the nozzle center line. It followed that, at the lower station, compared to the stationary status, the leading edge of the moving jet was deflected about 0.2 m backward and the trailing edge was deflected more than 0.34 m backward. Note that the jet traveled in the negative y-axis direction while the probes were set stationary at (z, y = 0) coordinates. The (z = 0, y = 0) coordinate corresponds to the stationary nozzle center line. This direction of travel, also indicated on the figure, might seem confusing if it were correlated with the tail of the moving jet. The confusion could be cleared out if one keeps in mind that those readings represent velocity measurements recorded at the (z, y = 0) probe coordinates while the nozzle center line was located at (z, y) coordinates. 3) The overall behavior of the 30 kPa controlled jet was similar to that of the non controlled jet indicating practically no noticeable effects of the lower controller pressures. The moderate controller pressure of 60 kPa appeared to have produced significant effects of velocity control; in magnitude, there was about 5 m/s reduction at the upper station and about 2 m/s reduction at the lower station. The effects on the shape of the jet are also clear; Because the controller jets were set across the nozzle travel axis, the ellipticity of jet was produced along the nozzle travel axis and resulted into significantly more elliptical geometry of the moving jet. 4) The motion and control effects are similarly apparent for both controller sizes, except for the more apparent structural disturbance of the jet, the D/1 controller effects were not much different from those of the D/2 controller which appeared to provide smoother control of the geometry of the moving jet. 5) The contour plots at the lower

station are wider, but weaker (smaller velocity magnitudes) than those at the upper station, indicating normal expansion of the moving controlled and non controlled jet.

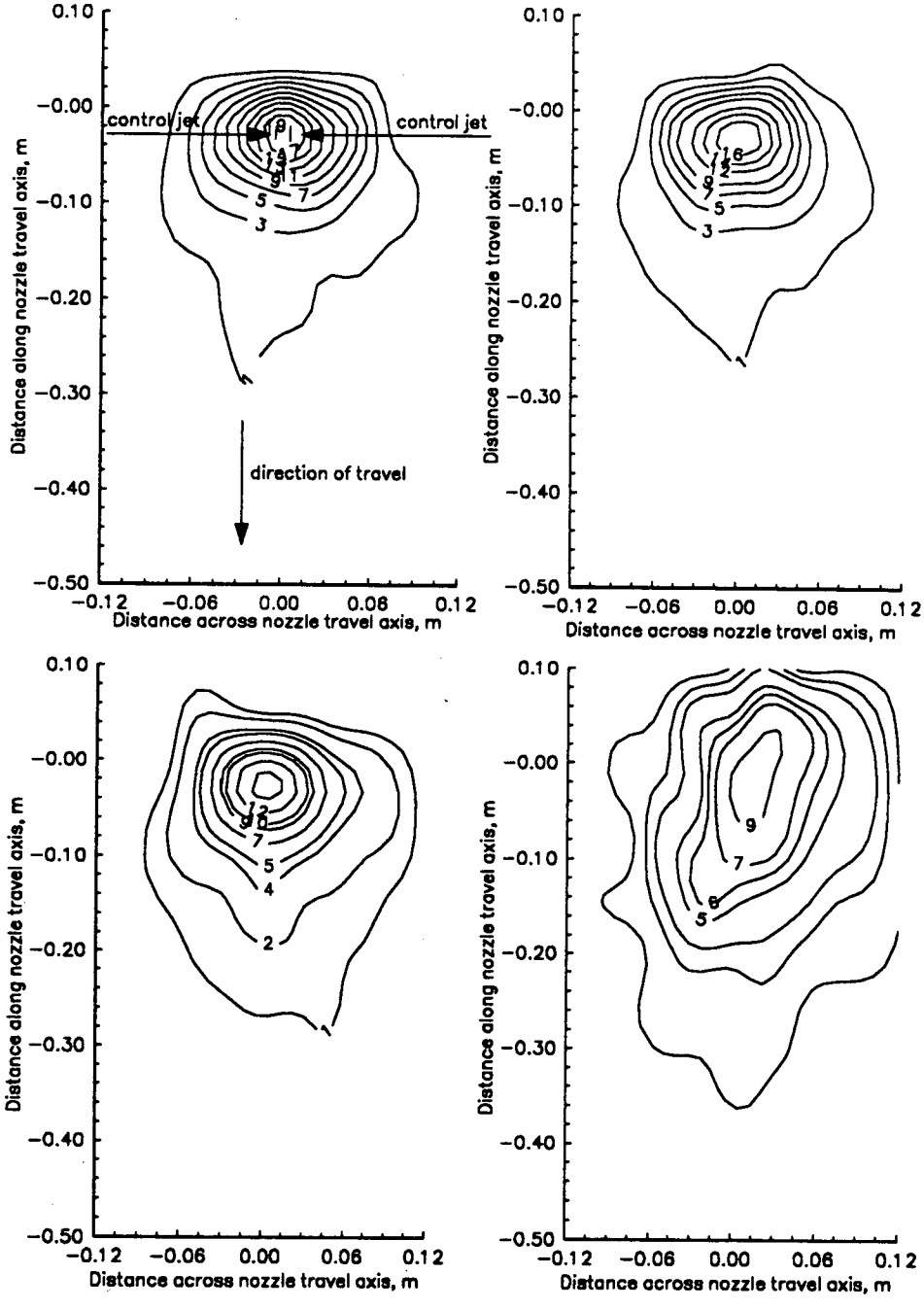

Figure 11. Contour plots (in m/s) of the observed velocity indicating the flow field shape of the moving jet at 0.3 m downstream for main jet pressure 275 kPa and D/1 control pressures: (a) 0 kPa, (b) 30 kPa, (c) 60 kPa, and (d) 90 kPa.

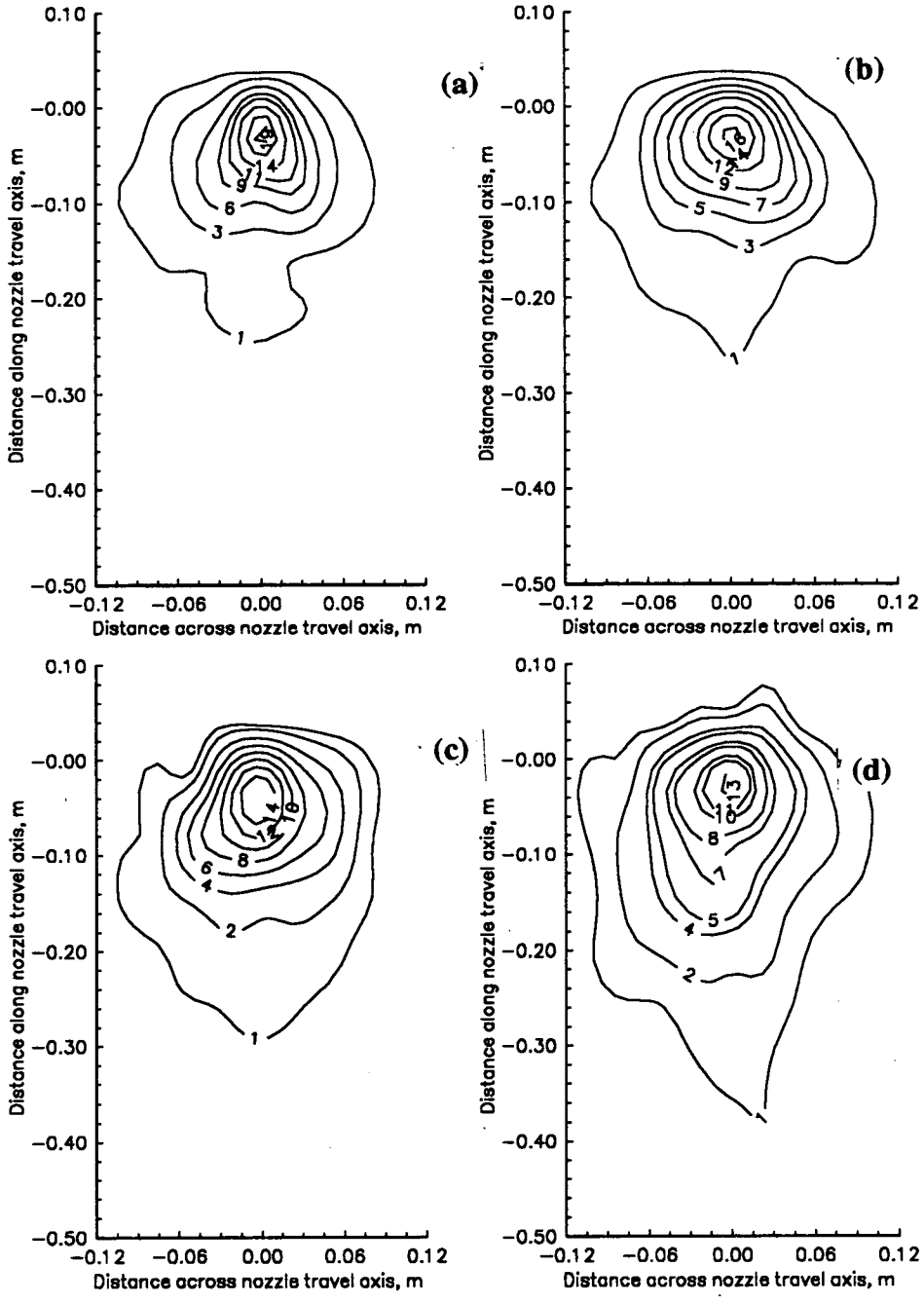

Figure 12. Contour plots (in m/s) of the observed velocity indicating the flow field shape of the moving jet at 0.3 m downstream for main jet pressure 275 kPa and D/2 control pressures: (a) 0 kPa, (b) 30 kPa, (c) 60 kPa, and (d) 90 kPa.

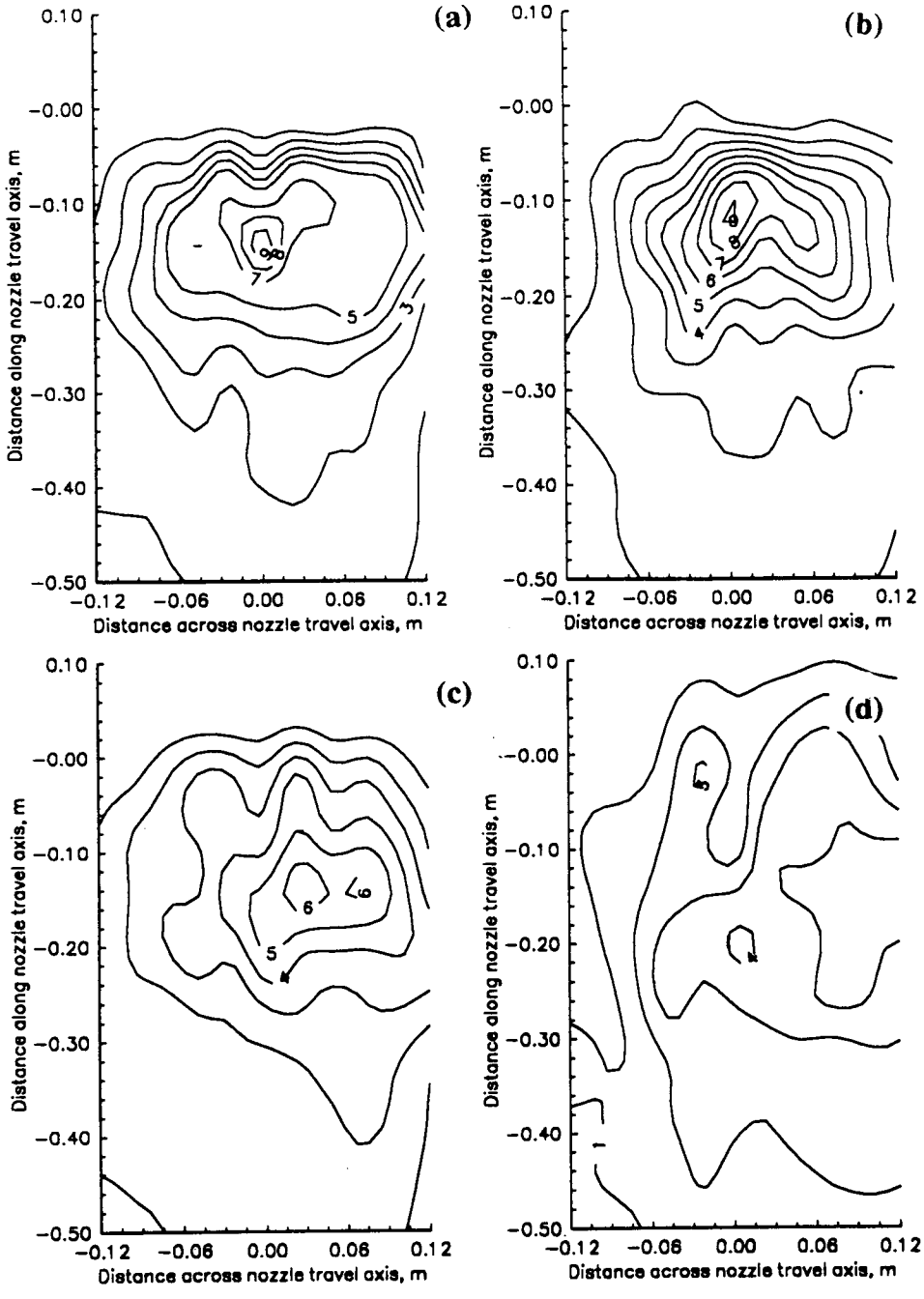

Figure 13. Contour plots (in m/s) of the observed velocity indicating the flow field shape of the moving jet at 0.6 m downstream for main jet pressure 275 kPa and D/1 control pressures: (a) 0 kPa, (b) 30 kPa, (c) 60 kPa, and (d) 90 kPa.

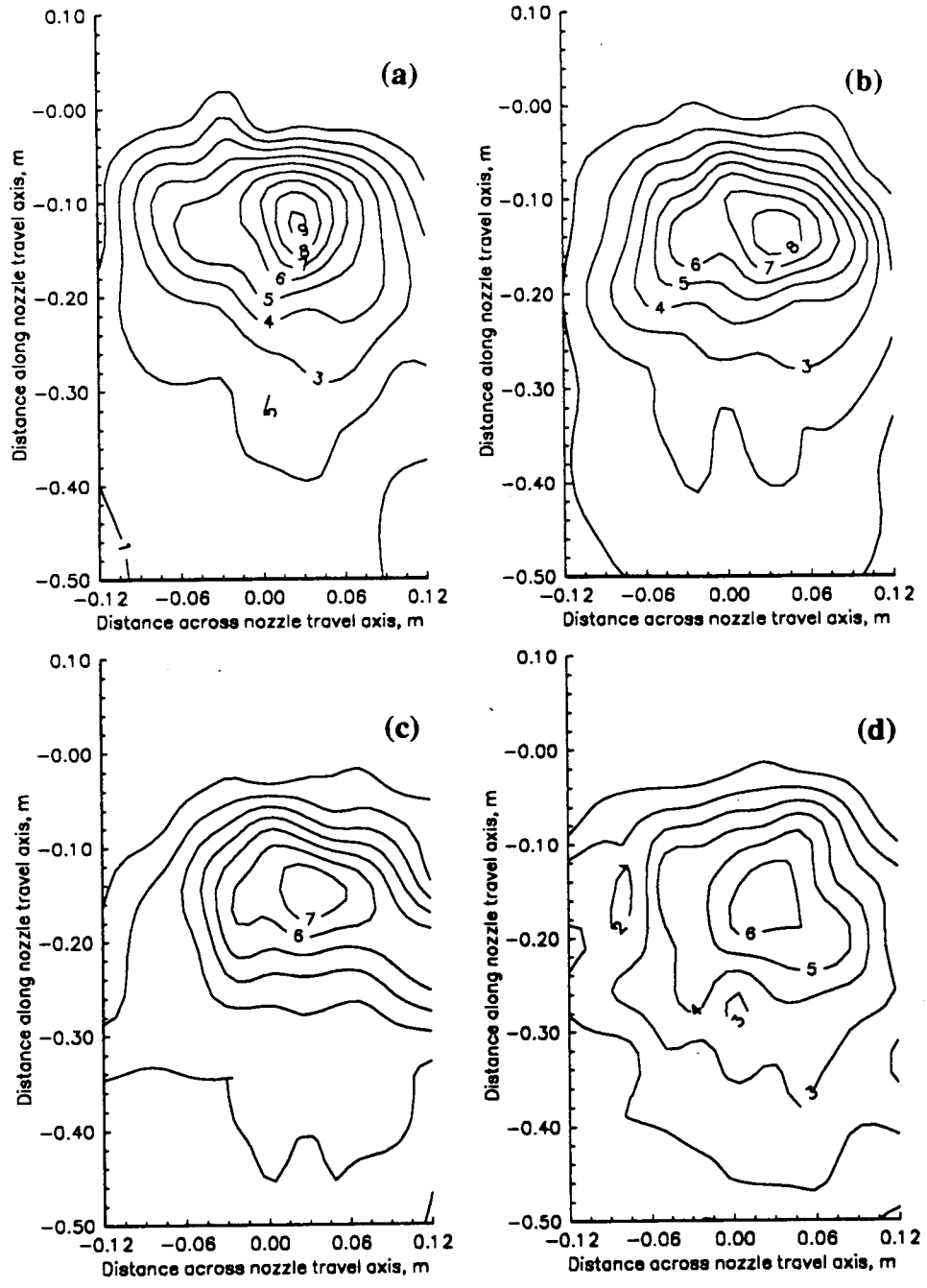

Figure 14. Contour plots (in m/s) of the observed velocity indicating the flow field shape of the moving jet at 0.6 m downstream for main jet pressure 275 kPa and D/2 control pressures: (a) 0 kPa, (b) 30 kPa, (c) 60 kPa, and (d) 90 kPa.

Phase 2. Canopy characterization, jet penetration and spray deposition (Objective 1)

Background. Behavior of the air flow within plant canopies is difficult to describe. Subsequently, reports of previous work are somewhat divergent in nature. Fundamental approaches, typically represented by work such as that of Bache (1979), have focused on low-momentum droplet fluxes similar to those from aerial spraying or natural convention processes driven by atmospheric air flow or boundary layer interactions between wind and plant canopies. Practical approaches, such as equipment performance testing (e.g., Randall, 1971; Furness and Pinczewski, 1985) have focused on particular canopies and machines and reported very specific results that are difficult to adapt to generic situations.

Mathematical and physical description of plant canopy structure and the corresponding influence on air-carrier flow is necessary for air penetration and spray deposition studies to be useful in process design. As a minimum, leaf area, expressed absolutely or as a non-dimensional index, and leaf area density, expressed as foliar area per until volume of enclosed canopy can provide objective measures of the plant characteristics. Analogies between air jet or spray penetration and attenuation of radiation, heat or moisture fluxes within canopies can be developed using a canopy resistance approach (Rosenberg, 1983) or an extinction approach (Gardner et al., 1985). The goals of this phase of the project were to develop simple and useful expressions for investigation of plant canopy structure, air-carrier penetration and distribution of spray deposition in a dense canopy. The specific goals were: 1) develop a simple, explicit mathematical model to describe the vertical distribution of foliar area and density within a plant canopy; 2) experimentally determine the penetration of an air jet, produced by an air-jet nozzle and control system and moving through a plant canopy; and, 3) determine the penetration and deposit of spray liquid delivered by the jet and describe the deposition using the plant model.

Experimental Apparatus and Procedures. Commercially-produced, potted chrysanthemums were used as the test canopy throughout the study. The chrysanthemums were grown in 15 cm diameter plastic pots with four plants within each pot. The plants were produced for the floral trade using growth and flowering control through photoperiod manipulation and manual disbudding. The canopy within each pot was shaped somewhat like an ellipsoid with approximate middle section dimensions of 32 x 28 cm and an approximate height of 30 cm.

Measurement of the plant foliar area was done by dividing the plant into 6 vertical zones with the height of each zone being 1/6 the plant height of the plant or approximately 5 cm. A digital indicating, micro-positioner was set at the top of the plant and zeroed. The positioner was moved downward by one zone height and all the plant leaves and stems above the positioner were removed. The projected area of the plant material removed from each zone was measured

using an optical planimeter. The vertically-projected area of each plant zone was estimated by measuring the major and minor axes of an ellipse surrounding the plant.

Air penetration into the plant canopy was investigated using the arrangement shown in Figure 15. A canopy bed was composed of 24 chrysanthemum pots arranged in a 3 x 8 pot array on 30 cm centers. The spacing resulted in a dense continuous plant canopy. The jet nozzle was positioned above the plant tops and directed vertically downward over the center of the plants in the center row of pots. The nozzle travelled along the 8 pot length of the bed at 1.5 m/s.

As the jet travelled over the fifth pot row, the air velocity at the top of and within the center pot was measured by hot-film probes positioned within the plant as shown in Figure 16. Probes were positioned at the top of the plant and at 5, 15 and 25 cm downward into the canopy. The 4-channel, constant-temperature hot-film anemometry system, discussed earlier, maintained the probes at 620^{o} K. Data collection commenced when the nozzle passed a proximity detector 0.2 m forward of the plant and continued for 1 s or 1.5 m of nozzle travel, allowing velocities during the approach, spraying interaction and departure of the jet to be recorded. The vertical array of velocity probes was positioned directly under the nozzle centerline and at 2, 4, 6, 8, 12 and 16 cm outward in both directions along the axis normal to nozzle travel; therefore, velocity was determined at 52 positions within each potted plant. Since 4 positions were sampled during each spray pass, 13 passes were required to characterize the flow within each sample plant.

Figure 15. Experimental apparatus consisting of plant canopy bed (center), spray carriage system (right), nozzle and control jets (top) and hot-film probes (in canopy) supported by a micropositioner (left).

Figure 16. Typical chrysanthemum canopy with hot-film probes at 0, 5, 15, and 25 cm downward in canopy.

Spray deposition was investigated using spray passes with the nozzle and control jets operating identically to the conditions used for the jet penetration study. Spray liquid, consisting of a solution of 2.5% w/w Zn and 0.05% v/v Triton X-100 surfactant, was supplied to the nozzle at 150 ml/min. After spraying, leaf samples were removed from 9 regions of the plant: three heights, 5, 10 and 25 cm downward from the plant top, and three horizontal positions, the center of the pot and 8 cm outward in each direction along the axis normal to nozzle travel. The leaf samples were washed with 100 ml of 0.26 N HCl solution and concentration of Zn in the wash solution determined by atomic absorption spectrophotometry. After washing, the area of each leaf sample was determined using an optical planimeter. Spray deposition was calculated and expressed as μl of spray liquid per cm^2 of leaf area.

The canopy penetration experiments were run at two nozzle-to-plant spacings, i.e., 30 and 60 cm and two orientations of control jets. The control jets were oriented in-line with the axis of nozzle travel and perpendicular to the axis of nozzle travel. The in-line or parallel orientation of the control jets allowed the normally circular jet to be widened and cover a greater spray swath. The perpendicular orientation allowed the jet to be narrowed and cover a smaller spray swath for an increased duration of spray time along the central axis.

Spray deposition experiments were run with both control jet orientations and a nozzle-to-plant spacing of 30 cm. Since spray deposition measurement required destruction of the plant, a new plant was required for each spray run.

Results and Discussion of Air and Spray Penetration Study. Attenuation of solar radiation within plant canopies has been extensively studied and provided an analogy for the penetration of an air jet and spray liquid into canopies. Sunlight dissipation within plant canopies is often described (Gardner et al., 1985) using the non-dimensional leaf area index, LAI, and a first order exponential decay model:

$$\frac{I_i}{I_0} = e^{-k(LAI)}, \qquad (18)$$

where, I_0 is the incident or source radiation flux above the canopy, I_i is the radiation beneath the i^{th} canopy layer and entering the $(i+1)^{th}$ layer, LAI is the cumulative leaf area index at the i^{th} canopy layer, and, k is the radiation extinction coefficient.

The model describes the radiation absorption of the canopy as a function of the cumulative leaf area index rather than the vertical depth (length dimension) into the canopy. Simple application of the model in the length domain requires a mathematical mapping or expression of cumulative leaf area index as a function of depth within plant canopy:

$$\Sigma LAI = f(z), \qquad (19)$$

where, z is the depth within the plant canopy in m, ΣLAI is the cumulative leaf area index (unitless) at depth z. Practically, the LAI was calculated for a given depth as the ratio of the enclosed leaf area to the projected local area of the plant at that depth. The projected local area was taken as the elliptical surface defined by the cross-widths of the plant at the given depth.

The function, f(z), of Equation 19 was determined by means of least squares fit of a logarithmic model to the observed data of cumulative leaf area index. The model chosen was:

$$\Sigma LAI = \alpha - \beta e^{-\lambda z}. \tag{20}$$

Plants typically grow more foliage in the upper region to maximize inception of sunlight. Cumulative LAI would increase rapidly in the upper regions of the plant and the rate of increase would slowly decrease to zero in lower regions of the plant. Equation 20 mathematically described such physical behavior. Mathematically, α is the asymptotic maximum value of cumulative LAI (also equal to the total LAI of the plant), α-β represents the nature of the curve fit since at depth z = 0, ΣLAI = 0 and α-β should equal zero, and λ represents the rate of LAI accumulation. Equation 20 was fit to observed data from the chrysanthemums and the parameter estimates and standard errors were:

$$\begin{aligned} &\alpha = 9.54 \ (1.75), \text{ unitless}, \\ &\beta = 11.47 \ (1.16), \text{ unitless}, \\ &\lambda = 5.44 \ (1.98), \ m^{-1}. \end{aligned} \tag{21}$$

Figure 17 shows the fit ($r^2 = 0.85$) of the model to the observed data.

While the above model expressed the total foliar area, it could not directly reveal insight into spatial density of foliage. Frankel (1986) developed a parameter, the leaf-area-volume index, LAVI, to describe local foliar density within a plant canopy; LAVI was defined as the leaf area within a given sample of plant foliar volume. In this study, LAVI at each interval downward through the chrysanthemum canopy was calculated as the ratio of the local leaf area to the volume defined by the local elliptical surface area of the plant and the depth interval within the plant canopy:

$$LAVI = \frac{Leaf\ Area}{(Local\ Area)\,\Delta z}. \tag{22}$$

A non-linear expression of a second order parabola,

$$LAVI = \mu + \chi(z - \tau)^2, \tag{23}$$

was developed to describe the vertical distribution of the LAVI. Typically, the LAVI starts low at the top of the plant because stems project new growth upward and the top of the plant is not a sharp boundary. The density increases to a maximum, μ, at a depth τ and then decreases. The model was fit to the data (Figure 18) and the parameter estimates and standard errors were:

$$\begin{aligned} &\mu = 31.9 \ (2.23), \ m^{-1}, \\ &\chi = -952 \ (239), \ m^{-2}, \text{ and,} \\ &\tau = 0.15 \ \ (0.01), \ m. \end{aligned} \tag{24}$$

The correlation coefficient of the fit was relatively low, $r^2 = 0.35$; however, the observed data showed the high variability and any model might appear weak. Comparison of the model in Figure 18 to a typical plant as in Figure 16 confirmed the model utility, especially since the model showed a maximum foliage density, μ at about half depth, τ in the plant. This was consistently noted in the observed data.

Air jet penetration was analyzed from the air velocity data recorded from within the plant as the nozzle passed overhead. The jet control system allowed a single nozzle to produce jets with different velocity, mass and momentum characteristics. An example velocity signature, taken along the jet travel centerline and at the top of the plant canopy prior to the jet entering the canopy is shown in Figure 19. The jet approach to, interaction with and departure from the plant can be clearly seen. Moreover, the influence of the control jets is also apparent; as the control jet pressure was increased and the jet was spread over a larger "footprint", the peak velocity decreased and the period of interaction increased. The jet shape and velocity distribution were also expressed in contour plots of the moving jet as shown in Figure 20. The jet nozzle and controller has been described earlier and a complete discussion of peak velocities, event duration and length scale (the integral of velocity with respect to time) of the moving jets appears in Ben Salem (1993).

Since the air jet was to be used for transport and deposition of spray droplets, total air mass, rather than velocity or flow length was selected as the primary response variable. Mass displacement past each sampling point was calculated as the product of the length scale and the vertically-projected area within which the probe was centered. The calculated mass displacement included velocity magnitude, event duration and sampling area effects. Mass attenuation within the plant canopy was investigated using an exponential decay function similar to Equation 18, or:

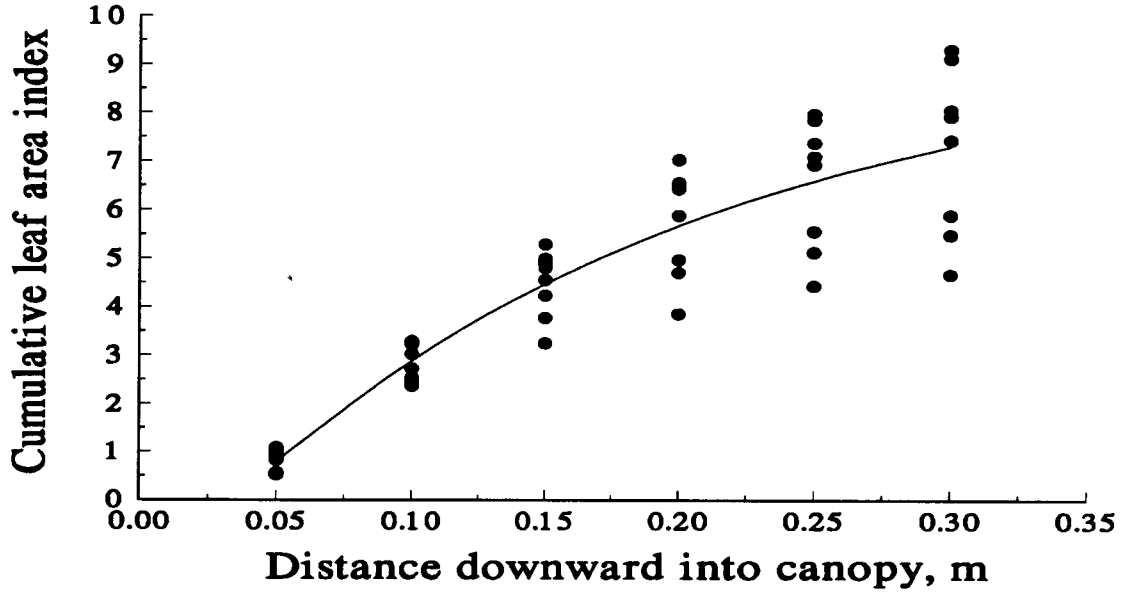

Figure 17. Cumulative leaf area index vs. vertical distance into canopy; •, observed; —, Eqn. 20.

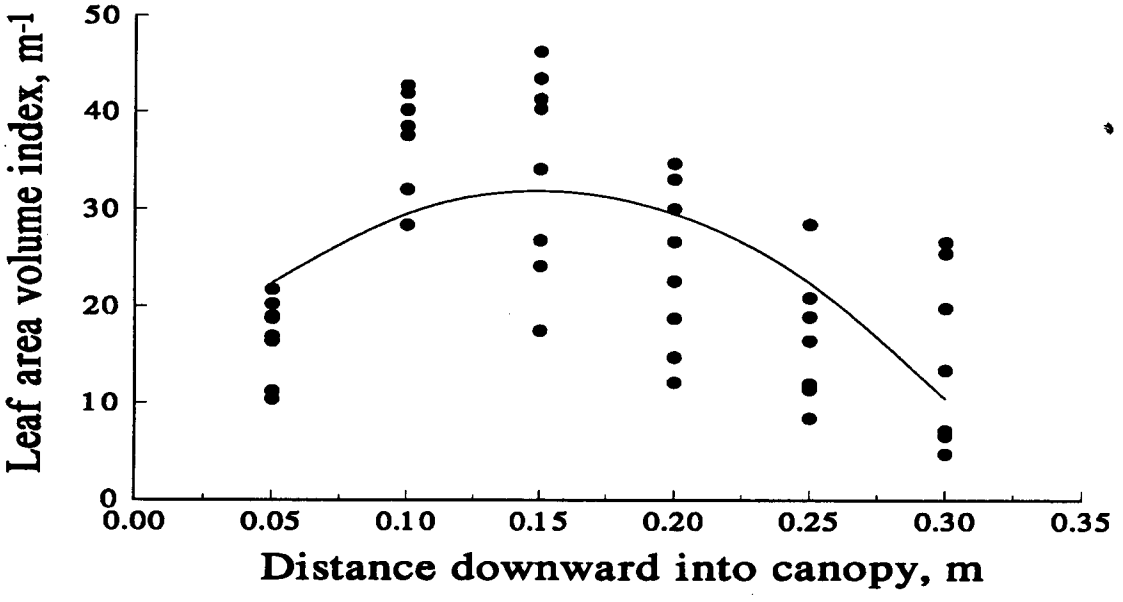

Figure 18. LAVI vs. vertical distance into canopy; •, observed; —, Eqn. 23.

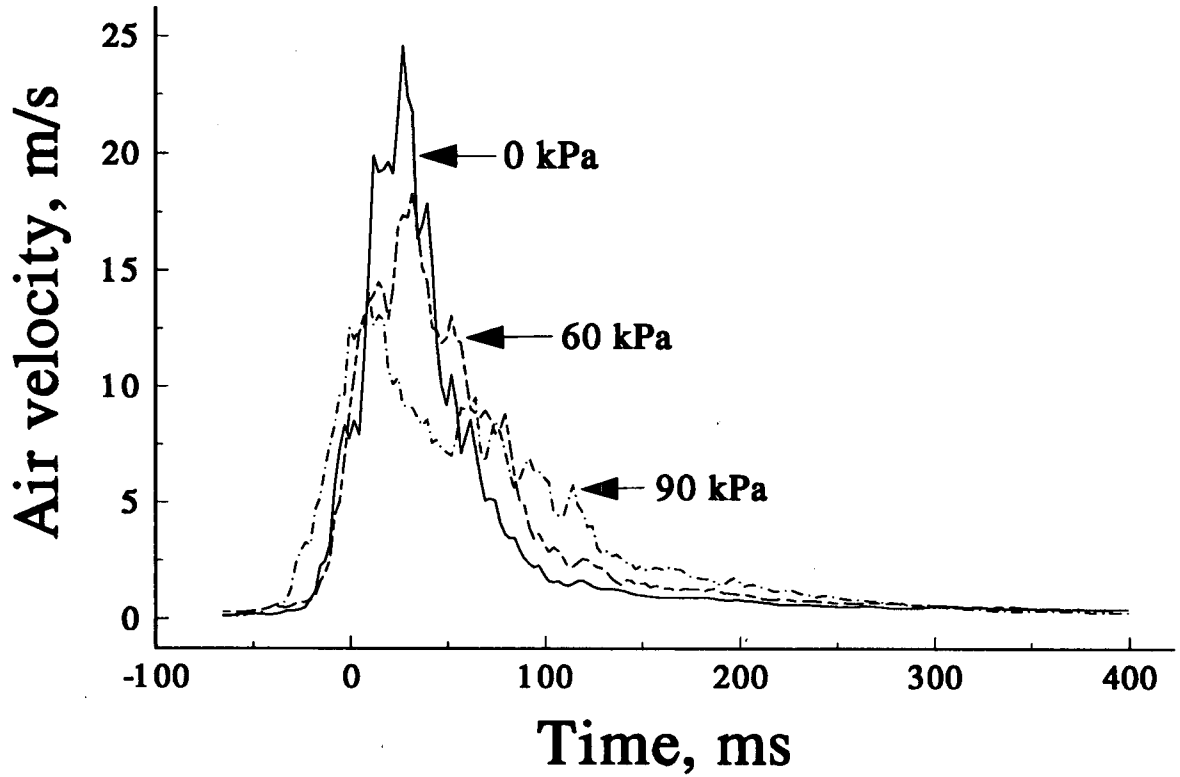

Figure 19. Velocity signature of controlled jet nozzle passing over a hot-film probe at 30 cm below the nozzle exit; time=0 when nozzle directly over probe; time<0 during approach; time>0 during departure. Main jet pressure at 275 kPa; travel speed of 1.5 m/s; control jet diameter of D/2; control jets oriented perpendicular to axis of travel.

$$\frac{Q(z)}{Q_0} = e^{-k_m f(z)}, \qquad (25)$$

where, Q(z) is the total air mass (g) flow measured at depth z (m), Q_0 is the total air mass (g) flow injected, at the top edge, into the plant canopy, k_m is a mass extinction coefficient, and, $f(z)$ is the relationship between ΣLAI and depth expressed in Eqns. 19 and 20.

Total air mass flow was calculated at all sampling locations and the four depth levels of the plant canopy. The resulting data was used to fit the model of Equation 25 by means of least squares methods. The total air mass flow injected to the plant canopy at the top edge, Q_0 was moved the right hand side of Equation 25 and statistically estimated as a model parameter. Statistical results are shown in Table 10, and plots of the total air mass flow vs. the depth within plant canopy are shown in Figure 21.

Ideally, the extinction coefficient would provide information on the attenuation of total air mass flow within the plant canopy and could provide a basis for comparison among treatments. Because of the negative sign in the exponent, larger k_m values indicate quicker flow attenuation and smaller k_m values indicate slower flow attenuation and therefore greater flow penetration within the plant canopy. Q_0, being air mass flow at the top edge of the canopy (z = 0), represents the amount of air mass flow injected into the canopy and reflected control jet effects on air mass input and ability to entrain air into the flow field.

Air mass flow rate input was found, for the 275 kPa nozzle main jet pressure, to be 4.42, 5.36. 5.98, and 6.54 g/s respectively, for 0, 30, 60, 90 kPa controller pressure. Since the nozzle was traveling at 1.5 m/s and the average plant width along the nozzle travel axis was 0.32 m, then the time of air flow over an individual plant would be 0.22 s. The total air mass input into the flow field at the nozzle exit would be 0.97, 1.18, 1.32 and 1.44 g respectively, for 0, 30, 60, and 90 kPa controller pressures. The total air mass injected into the plant canopy by the same treatments, at perpendicular control jet orientation, was found to be 33, 34, 38, and 51 grams. It was apparent from total air mass, Q_0 that increasing control jet pressure increased entrainment of ambient air into the flow field.

The simple exponential model of Equation 25 fit the observed data moderately well as indicated by the standard errors of the parameter estimates and the r^2 values. Increasing control jet pressure, which effectively increased the mass flux and decreased the velocity of the jet, generally increased foliar attenuation of the mass.

Analogously to air flow, the spray penetration within plant canopy was characterized by modeling the vertical distribution of liquid deposition on the plant foliage. Spray deposition was partitioned into the horizontal regions of the plant centerline directly underneath the nozzle jet

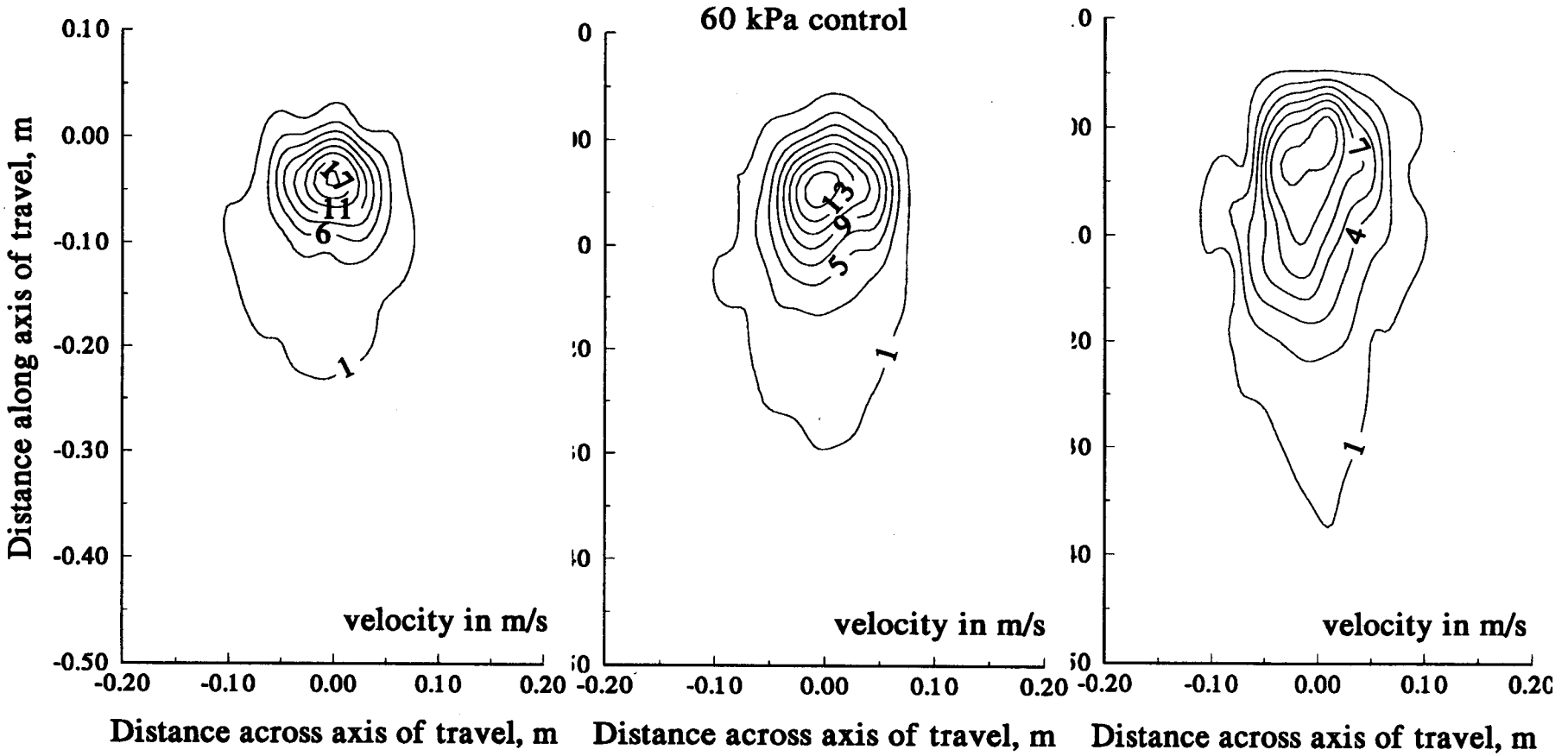

Figure 20. Velocity profile of controlled jet nozzle passing over a hot-film probe at 30 cm below the nozzle exit. Travel speed of 1.5 m/s; main jet pressure at 275 kPa; control jet diameter of D/2; control jet pressures of: 0 kPa (left), 60 kPa (center), and 90 kPa (right); control jets perpendicular to axis of travel.

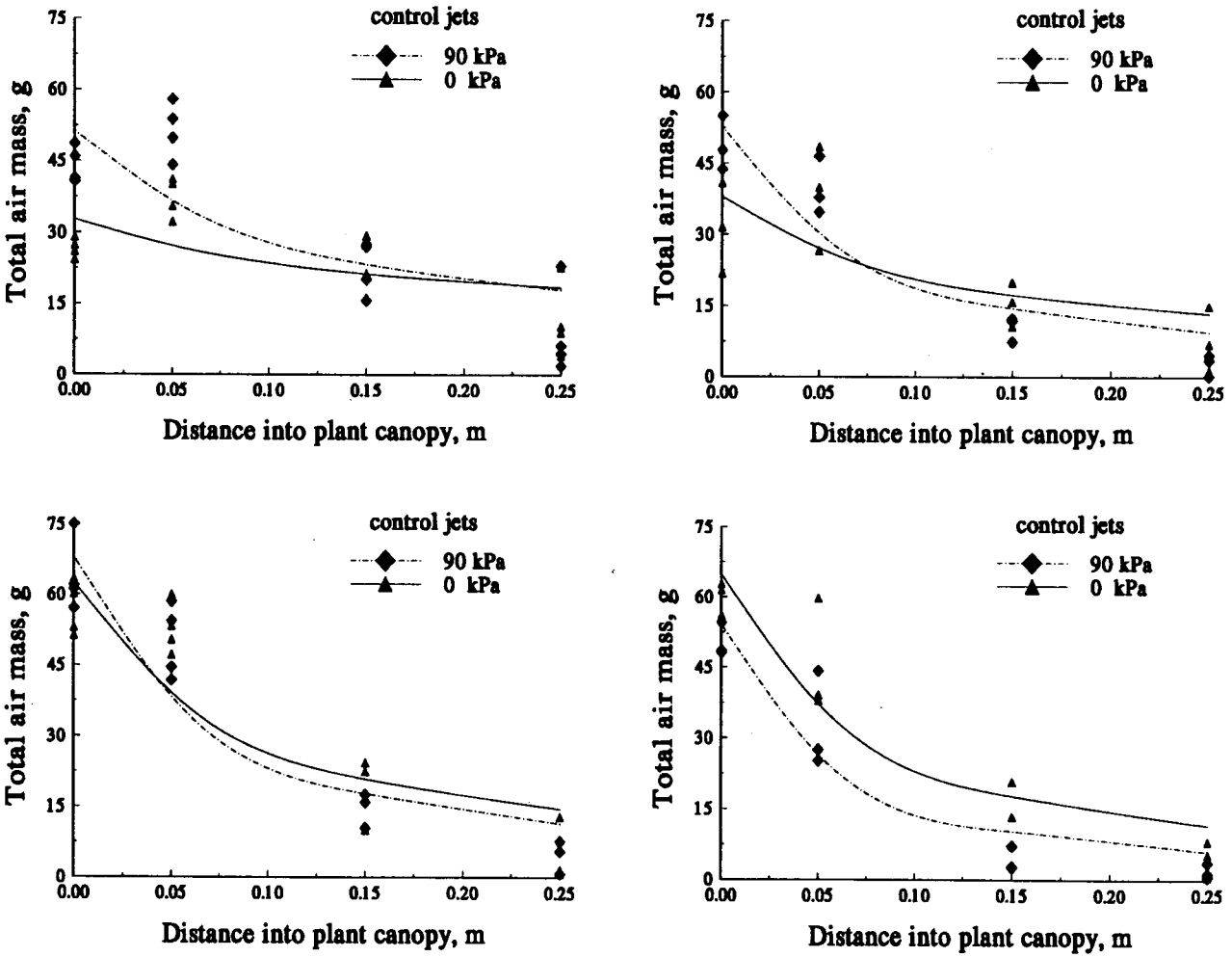

Figure 21. Attenuation of air mass moving through plant canopy from controlled and non controlled jets. Nozzle-to-plant spacing of 30 cm (top) and 60 cm (bottom); control jets oriented perpendicular to axis of travel (left) and along axis of travel (right).

and the left and right regions along an axis normal to the axis of nozzle travel. The spray deposition attenuation model was of the form:

$$\frac{SD(z)}{SD_{0.05}} = e^{-ks(f(z)-f(0.05))}, \qquad (26)$$

where,

SD(z) is the liquid spray deposit ($\mu l/cm^2$) at depth z (m), $SD_{0.05}$ is the liquid spray deposit at the top plant canopy (z = 0.05 m), f(z) is the foliage function described by Equation 20, and k_S is the extinction coefficient. Equation 26 was fitted to the observed data by least squares methods. The liquid spray deposit at the top edge of the plant canopy, $SD_{0.05}$, was moved to the right hand side of Equation 26 and statistically estimated rather than using the observed values.

Statistical results are shown in Table 11; plots of the liquid spray deposit vs. the depth within plant canopy are shown in Figures 22 and 23. Again, because of the negative sign in the exponent, larger k_S values would indicate more rapid spray attenuation and smaller k_S values would indicate slower spray attenuation and therefore, more uniform spray penetration within the plant. $SD_{0.05}$, the quantity of spray intercepted by the top zone of the plant, set a basis for comparison among jets due only to variation of spray jet structure because at the top zone of the plant (z = 0.05m), the canopy structure effects were yet to effect penetration.

Based on correlation coefficients and parameter estimates and standard errors, the model of Equation 26 fit the overall observed data moderately well, especially in the center region of the plant. A moderate level of jet shaping, i.e., 60 kPa control jet pressure, reduced the sharp gradient of spray deposition normal to the axis of travel; this was shown by the improved uniformity of $SD_{0.05}$ estimates for the center, left and right plant regions. Vertical attenuation of the spray deposition was greater for higher control jet pressures; this was consistent with the greater attenuation of air jet penetration found in earlier phases of the study.

Conclusions. Distribution of foliar area and density within a plant canopy were well described by relatively simple, non-linear expressions. Air jet penetration and spray deposition were modelled using a non-dimensional parameter, accumulated leaf area index, instead of linear distance into the canopy. A first-order, exponential decay, similar to the classic radiation extinction expression, was developed for air mass penetration and spray deposition. The expressions closely described observed data. The extinction rate of spray deposition was greater than that of air mass movement. Alternation of jet characteristics such as velocity profile and shape did not significantly change the spray deposition behavior. The difficulty of achieving spray deposition in lower regions of dense plant canopies was clearly demonstrated; deposition

in the upper plant regions was typically one order of magnitude greater than deposition in lower regions.

Table 10. Parameter estimates from the first-order, exponential decay model of total air mass flow downward through the plant canopy.

Nozzle Height m	Main Jet Pressure kPa	Control Jet Pressure kPa	Q_0 g	Std. Error of Q_0 g	k_m	Std. Error of k_m	r^2
			Orientation of Control Jets Perpendicular To Travel Axis				
.3	275	0	32.73	3.42	0.14	0.049	0.46
.3	275	30	32.93	3.84	0.15	0.055	0.41
.3	275	60	38.44	4.08	0.20	0.059	0.57
.3	275	90	51.31	4.40	0.25	0.055	0.73
.6	275	0	62.56	3.84	0.36	0.053	0.88
.6	275	30	64.17	4.05	0.36	0.055	0.88
.6	275	60	64.05	3.01	0.42	0.047	0.94
.6	275	90	68.00	3.52	0.45	0.056	0.93
			Orientation of Control Jets Along Travel Axis				
.3	275	0	37.91	4.51	0.26	0.077	0.60
.3	275	30	39.78	4.28	0.26	0.070	0.65
.3	275	60	46.55	4.78	0.31	0.073	0.73
.3	275	90	52.66	3.03	0.43	0.059	0.91
.6	275	0	64.83	3.94	0.43	0.063	0.90
.6	275	30	67.79	3.89	0.46	0.064	0.85
.6	275	60	66.71	4.24	0.48	0.074	0.90
.6	275	90	54.04	3.27	0.58	0.087	0.92

Table 11. Parameter estimates from the first-order, exponential decay model of liquid spray deposition downward through the plant canopy.

Plant Region	Main Jet Pressure kPa	Control Jet Pressure kPa	$SD_{0.5}$ $\mu l/cm^2$	Std. Error of $SD_{0.5}$ $\mu l/cm^2$	k_s	Std. Error of k_s	r^2
Orientation of Control Jets Perpendicular To Travel Axis							
Left	275	0	0.048	0.010	0.194	0.094	0.28
	275	30	0.118	0.012	0.315	0.072	0.72
	275	60	0.126	0.015	0.374	0.105	0.68
	275	90	0.104	0.007	0.523	0.119	0.87
Center	275	0	0.488	0.039	0.326	0.059	0.82
	275	30	0.485	0.052	0.459	0.138	0.79
	275	60	0.359	0.032	0.528	0.151	0.95
	275	90	0.302	0.011	0.531	0.064	0.92
Right	275	0	0.118	0.013	0.428	0.122	0.73
	275	30	0.116	0.019	0.402	0.168	0.52
	275	60	0.136	0.014	0.406	0.104	0.75
	275	90	0.131	0.014	0.421	0.114	0.75
Orientation of Control Jets Along Travel Axis							
Left	275	0	0.048	0.010	0.194	0.094	0.28
	275	30	0.063	0.012	0.212	0.090	0.35
	275	60	0.119	0.012	0.443	0.117	0.78
	275	90	0.091	0.008	0.457	0.109	0.82
Center	275	0	0.488	0.039	0.326	0.059	0.82
	275	30	0.342	0.032	0.447	0.113	0.74
	275	60	0.213	0.009	0.475	0.057	0.82
	275	90	0.086	0.005	0.512	0.088	0.97
Right	275	0	0.118	0.013	0.428	0.122	0.73
	275	30	0.169	0.019	0.386	0.105	0.72
	275	60	0.164	0.012	0.515	0.122	0.86
	275	90	0.087	0.011	0.472	0.171	0.68

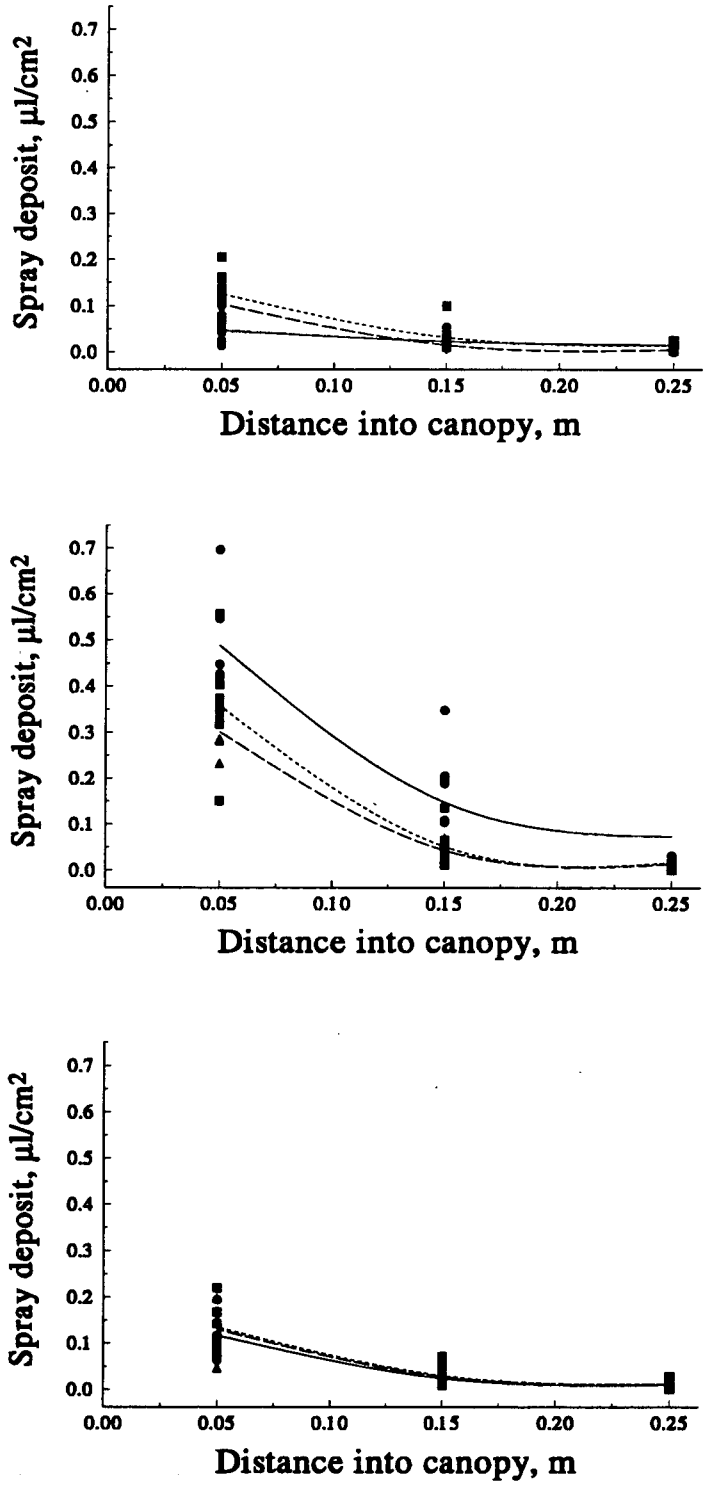

Figure 22. Attenuation of spray deposit within plant canopy; left (top plot), center (middle plot) and right (bottom plot) portions of plant. Main jet pressure of 275 kPa; control jet diameter of D/2; nozzle-to-plant spacing of 30 cm; control jets oriented perpendicular to axis of travel.

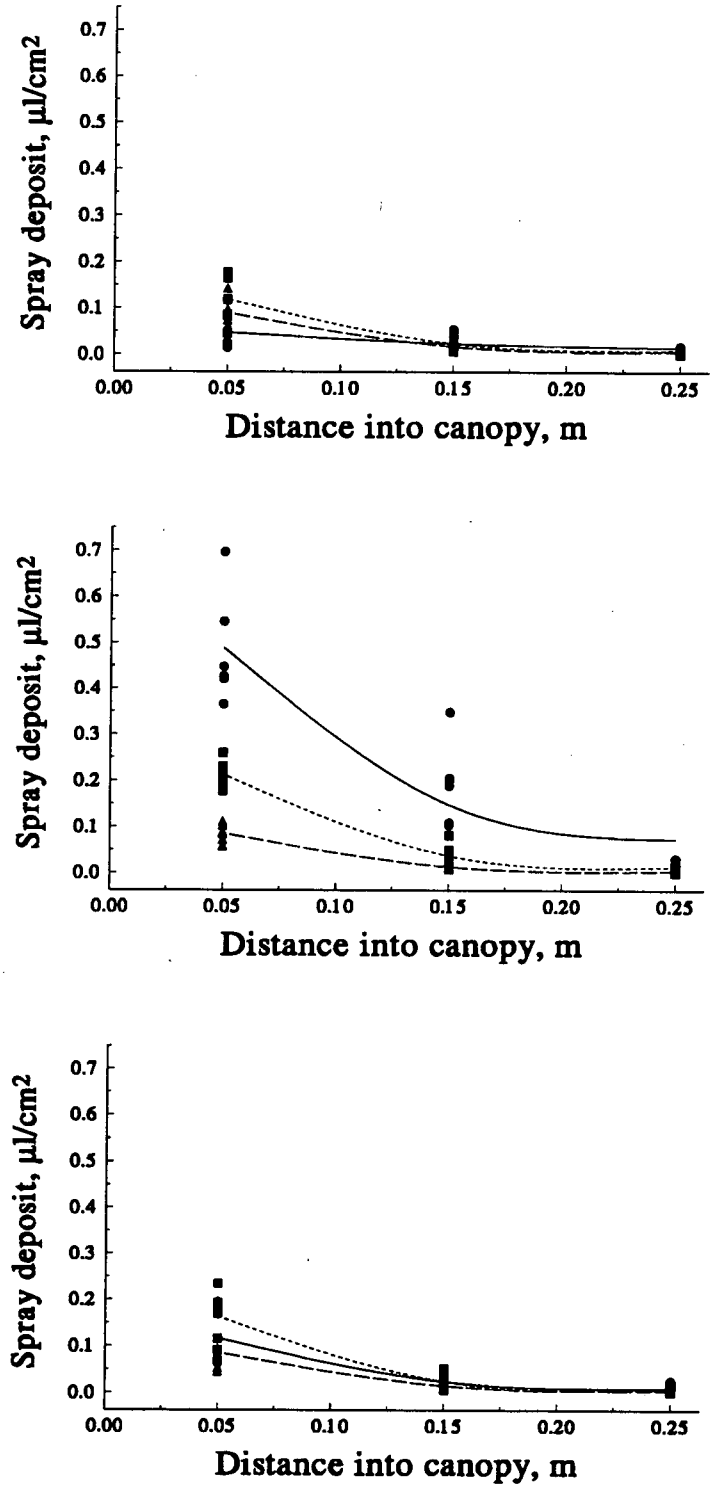

Figure 23. Attenuation of spray deposit within plant canopy; left (top plot), center (middle plot) and right (bottom plot) portions of plant. Main jet pressure of 275 kPa; control jet diameter of D/2; nozzle-to-plant spacing of 30 cm; control jets oriented along axis of travel.

References.

Abramovich, G.N. 1963. The theory of turbulent jets. MIT Press. Cambridge, Mass. 671 pp.

Bache, D.H. 1979. Particle transport within plant canopies - I. A framework for analysis. Atmos. Environ. 13:1257-1262.

Ben Salem, E. 1993. Spray target architecture and turbulent transport in air-carrier chemical application systems. Unpublished Ph.D. Dissertation. Biological and Agricultural Engineering Department, University of California, Davis, CA. 248 pp.

Brazee, R.D.; R.D., Fox; D.L., Reichard and F.R., Hall. 1981. Turbulent jet theory applied to air sprayers. Trans. of ASAE 24(2):266-272.

Davis, M.R. 1982. Variable control of jet decay. AIAA Journal 20:606-609.

Ffowcs Williams, J.E. 1973. Noise mechanisms. AGARD Conference Proceedings No. 131. NATO Advisory Group for Aerospace Research and Development. Brussels, Belgium. Sept. 19-21, 1973.

Fox, R.D.; R.D., Brazee and D.L., Reichard. 1985. A model study of the effect of wind on air sprayer jets. Trans. of ASAE 28(1):83-88.

Frankel, H. 1986. Pesticide application, technique and efficiency. In: Pali, J. and R. Ausher (Eds.) Advisory work in crop pest and disease management. Springer Verlag, New York, NY. pp. 132-160.

Furness, G.O. and W.V., Pinczewski. 1985. A comparison of the spray distribution obtained from sprayers with converging and diverging air jets with low volume air assisted spraying on citrus and grapevines. J. Ag. Eng. Res. 32(4):291-310.

Gardner, F.P.; R.B. Pearce and R.L. Mitchell. 1985. Physiology of crop plants. Iowa State University Press. Ames, IA. 327 pp.

Giles, D.K.; E., Ben Salem and N., Bagheri. 1991. Turbulent jet flow characteristics of a dual-port, air-atomization spray nozzle. J. Ag. Eng. Res. 49:133-149.

Randall, J.M. 1971. The relationships between air volume and pressure on spray distribution in fruit trees. J. Ag. Eng. Res. 16(1):1-31.

Rosenberg, N.J.; B.L., Blad and S.B., Verma. 1983. Microclimate: The biological environment. John Wiley and Sons Inc.

Salyani, M. and J.D., Whitney. 1991. Effect of oscillators on deposition characteristics of an airblast sprayer. Trans. of ASAE 34(4):1618-1622.

Cooperation:

Development of the pneumatic nozzle control system and the air flow measurement apparatus was accomplished at UC-Davis, USA. Foliar canopy measurement techniques were developed at ARO, Israel. LAVI measurements in the U.S. were taken using techniques developed At ARO. Spray deposition measurements, done in the U.S. were guided by Israeli techniques. Both Principal Investigators visited each other's laboratories for project planning and discussion of results.

Evaluation of Achievements:

The project objectives were met. A non-invasive, air-jet control system was developed and evaluated. The technique allows real time control of spray cloud characteristics. While effective, the technique requires significant pneumatic power and air mass input. Future study should be directed toward refining the technique to reduce the power requirements. An analogy between radiation attenuation in crop canopies and attenuation of air jet mass and momentum and resulting spray deposition as developed. The mathematical model expressing the analogy is simple, explicit and accurate. The technique facilitates straighforward estimation of spray deposition in dense foliar canopies.

Publications:

Giles, D.K., E. Ben Salem and N. Bagheri. 1991. Turbulent jet flow characteristics of a dual-port, air-atomization spray nozzle. J. Agric. Engng. Res. 49:133-149.

Ben Salem, E. and D.K. Giles. 1993. Air-carrier penetration and spray deposition in dense floral canopies. Paper No. 931006. Presented at 1993 International Summer Meeting of the American Society of Agricultural Engineers. June, 1993. Spokane, WA. ASAE, St. Joseph, MI.

Ben Salem, E. Spray target architecture and turbulent transport in air-carrier chemical application systems. 1993. Ph.D. Thesis. Department of Biological & Agricultural Engineering, University of California, Davis. Davis, CA.